Two self-similar Reynolds-stress transport models with anisotropic eddy viscosity

Brandon E. Morgan ⬤, Kevin Ferguson ⬤, and Britton J. Olson

Lawrence Livermore National Laboratory, Livermore, California 94550, USA

Two Reynolds-averaged Navier-Stokes models with full Reynolds-stress transport (RST) and tensor eddy viscosity are presented. These new models represent RST extensions of the k-$2L$-a-$\mathcal{C}$ and k-ϕ-L-a-$\mathcal{C}$ models by Morgan [Phys. Rev. E **103**, 053108 (2021); Phys. Rev. E **105**, 045104 (2022)]. Self-similarity analysis is used to derive constraints on model coefficients required to reproduce expected growth parameters for a variety of canonical flows, including Rayleigh-Taylor (RT) and Kelvin-Helmholtz (KH) mixing layers. Both models are then applied in one-dimensional simulation of RT and KH mixing layers, and the expected self-similar growth rates and anisotropy are obtained. Next, models are applied in two-dimensional simulation of the so-called "tilted rocket rig" inclined RT experiment [J. Fluids Eng. **136**, 091212 (2014)] and in simulation of a shock-accelerated localized patch of turbulence. It is found that RST is required to capture the qualitative growth of the shock-accelerated patch, and an anisotropic eddy viscosity provides substantial improvement over a Boussinesq treatment for the tilted rocket rig problem.

I. INTRODUCTION

Accurate prediction of turbulent mixing is important in a variety of applications, including in design for inertial confinement fusion (ICF) targets [1,2]. In ICF, turbulent mixing of heavy ablator material into light gas is primarily driven by Rayleigh-Taylor (RT) [3,4] and Richtmyer-Meshkov (RM) [5,6] instabilities. Reviews by Zhou [7,8], Banerjee [9], and Schilling [10] provide good overview of the current state of the art in understanding and modeling of RT and RM instabilities. However, localized sources of asymmetry such as fill tube perturbations, capsule supports, and x-ray shadowing can also contribute to the overall amount of turbulent mixing [11–15]. In some cases, these localized asymmetries may become significant enough that they cannot be neglected, and in these cases it is possible that a Boussinesq Reynolds-averaged Navier-Stokes (RANS) model would fail to accurately capture the impact of such features. For this reason, it is desirable to develop and assess non-Boussinesq models that might better capture the evolution of localized anisotropies.

Over the years, significant effort has been applied to the development and improvement of RANS models for turbulent mixing [16–41]. While some of the previous work has focused on development of Reynolds-stress transport (RST) modeling approaches (e.g., the BHR-3 [23,27], BHR-4 [39], and GSG [19,22,24] models), much of the previous work on RANS modeling for turbulent mixing has focused on the Boussinesq-type Reynolds stress approach where the Reynolds stresses R_{ij} are approximated according to

$$-\overline{\rho}R_{ij} \approx 2\mu\widetilde{S}_{ij} - \frac{2}{3}\overline{\rho}k\delta_{ij}, \qquad (1)$$

where μ is a scalar eddy viscosity, $\widetilde{S}_{ij}$ is the deviatoric rate-of-strain tensor, $\overline{\rho}$ is the Reynolds-averaged density, k is the turbulence kinetic energy (TKE), and δ_{ij} is the Kronecker delta. Even among previous RST models such as BHR-3 and BHR-4, it is common to utilize an isotropic, scalar eddy

viscosity of the form

$$\mu = C_\mu \overline{\rho} L \phi, \qquad (2)$$

where C_μ is a model constant, L is a characteristic turbulence length scale, and ϕ is a characteristic turbulence velocity scale. Often L and ϕ are obtained from other turbulence variables such as k or the TKE dissipation rate ε. For instance, in a BHR or k-L-type model, $\phi \equiv \sqrt{k}$, and in a k-ε model, $L \equiv \frac{k^{3/2}}{\varepsilon}$.

An alternative approach that may be more likely to capture local anisotropies is to formulate a tensor eddy viscosity according to

$$\mu_{ij} = C_\mu \overline{\rho} L \phi_{ij}, \qquad (3)$$

where ϕ_{ij} is now a tensor that can incorporate anisotropy into gradient diffusion closures involving μ_{ij}. In the GSG model, for instance, $L \equiv \frac{k^{3/2}}{\varepsilon}$ and $\phi_{ij} \equiv \frac{R_{ij}}{\sqrt{k}}$. Of course, a tensor eddy viscosity of the form of Eq. (3) is not readily compatible with the Boussinesq Reynolds stress closure of Eq. (1). So Eq. (3) is typically used in conjunction with an RST formulation for the Reynolds stresses.

Self-similarity analysis is a powerful tool that can be used to determine analytical constraints on RANS model coefficients necessary to reproduce expected self-similar growth behavior in canonical problems such as one-dimensional (1D) RT, RM, and Kelvin-Helmholtz (KH) turbulent mixing layers [20,26,29]. By assuming an ansatz that turbulence variables can be separated into a time-varying component and a self-similar spatial component, it becomes possible to reduce the coupled partial differential equation system to an ordinary differential equation system, and the assumed self-similar profiles are recovered. This approach has been used previously to derive constraints for many k-L-type models [20,26,29,30, 36–38,40,41], the k-ε model [42], and the BHR-2 model [21,43]. Although most applications of self-similarity

analysis are limited to assumptions of low-order spatial profiles (i.e., linear concentration profiles and a quadratic TKE profile), the k-ϕ-L-a-$\mathcal{C}$ model [38,40] achieves high-order spatial profiles by introducing an additional transport equation for a turbulence velocity ϕ. To the knowledge of the authors, the self-similarity approach has not yet been applied to any RST-type models.

The aim of the present work is to develop RST extensions to the k-$2L$-a-$\mathcal{C}$ [37,40] and k-ϕ-L-a-$\mathcal{C}$ [38,40] models which can be constrained through self-similarity analysis and can utilize a tensor eddy viscosity of the form of Eq. (3). In Sec. II the governing equations for the two new models, termed the R-$2L$-a-$\mathcal{C}$ and the R-ϕ-$2L$-a-$\mathcal{C}$ models, are presented. Next, in Sec. III self-similarity analysis is presented for the R-ϕ-$2L$-a-$\mathcal{C}$ model, and model coefficients are determined based on self-similarity constraints. Additional analysis for the R-$2L$-a-$\mathcal{C}$ is included in Appendix. Then in Sec. IV both models are applied to a series of test problems, including 1D RT, quasi-1D KH, inclined RT in the two-dimensional (2D) "tilted rocket rig" problem [44–47], and the 2D shock-accelerated patch of turbulence problem described by Olson and Williams [48]. These test problems demonstrate that the expected self-similar profiles and growth rates are recovered, and the new RST models with anisotropic eddy viscosity are demonstrated to outperform Boussinesq models in areas of localized anisotropy. Finally in Sec. V conclusions are drawn, and recommendations are made for the direction of future work.

II. MODEL EQUATIONS

A. The R-$2L$-a-$\mathcal{C}$ model

The R-$2L$-a-$\mathcal{C}$ model is an RST extension of the k-$2L$-a-$\mathcal{C}$ model. It is derived from the compressible RANS equations for a multicomponent, nonreactive gas mixture. In the present work, an overbar denotes Reynolds averaging, and a tilde denotes mass-weighted (Favre) averaging. An arbitrary scalar f is decomposed as

$$f = \overline{f} + f' = \widetilde{f} + f'', \tag{4}$$

where the Favre average is related to the Reynolds average through the density, ρ, according to

$$\widetilde{f} = \frac{\overline{\rho f}}{\overline{\rho}}. \tag{5}$$

The Reynolds stress tensor, mass-flux velocity vector, and mass fraction covariances are defined, respectively, in terms of the velocity vector, u_i, and the component mass fraction, Y_α, by

$$R_{ij} \equiv \widetilde{u_i'' u_j''}, \tag{6a}$$

$$a_i \equiv -\overline{u_i''}, \tag{6b}$$

$$\mathcal{C}_{\alpha\beta} \equiv \widetilde{Y_\alpha'' Y_\beta''}. \tag{6c}$$

Equations (7)–(15) below summarize the R-$2L$-a-$\mathcal{C}$ model, where μ_{ij} is the eddy viscosity, g_j is the gravitational acceleration vector, e is the specific internal energy, L_t is the turbulence transport length scale, and L_d is the turbulence destruction length scale. The model coefficients C_{R1}, C_{R2}, C_{R3},

C_{R4}, C_{L1}, C_{L2t}, C_{L3t}, C_{L2d}, C_{L3d}, C_A, C_{C1}, C_{C2}, C_{C3}, N_e, N_Y, N_R, N_{Lt}, N_{Ld}, N_a, and N_C, are determined through similarity analysis as described in Appendix. The model equations are

$$\frac{D\overline{\rho}}{Dt} = -\overline{\rho} \frac{\partial \widetilde{u}_i}{\partial x_i}, \tag{7}$$

$$\overline{\rho} \frac{D\widetilde{Y}_\alpha}{Dt} = \frac{\partial}{\partial x_i}\left(\frac{\mu_{ij}}{N_Y}\frac{\partial \widetilde{Y}_\alpha}{\partial x_j}\right), \tag{8}$$

$$\overline{\rho} \frac{D\widetilde{u}_j}{Dt} = -\frac{\partial \overline{p}}{\partial x_j} - \frac{\partial}{\partial x_i}(\overline{\rho} R_{ij}) + \overline{\rho} g_j, \tag{9}$$

$$\overline{\rho} \frac{D\widetilde{e}}{Dt} = -\overline{p}\frac{\partial \widetilde{u}_i}{\partial x_i} - a_i \frac{\partial \overline{p}}{\partial x_i}$$
$$+ C_{R4}\overline{\rho}\frac{(2k)^{3/2}}{L_d} + \frac{\partial}{\partial x_i}\left(\frac{\mu_{ij}}{N_e}\frac{\partial \widetilde{e}}{\partial x_j}\right), \tag{10}$$

$$\overline{\rho} \frac{DR_{ij}}{Dt} = (1 - C_{R1})\left(a_i \frac{\partial \overline{p}}{\partial x_j} + a_j \frac{\partial \overline{p}}{\partial x_i}\right)$$
$$+ (C_{R2} - 1)\overline{\rho}\left(R_{ik}\frac{\partial \widetilde{u}_j}{\partial x_k} + R_{jk}\frac{\partial \widetilde{u}_i}{\partial x_k}\right)$$
$$- C_{R3}\overline{\rho}\frac{\sqrt{2k}}{L_d}\left(R_{ij} - \frac{1}{3}R_{kk}\delta_{ij}\right)$$
$$+ \frac{2}{3}\left(C_{R1}a_k\frac{\partial \overline{p}}{\partial x_k} - C_{R2}\overline{\rho}R_{mk}\frac{\partial \widetilde{u}_m}{\partial x_k} - C_{R4}\overline{\rho}\frac{(2k)^{3/2}}{L_d}\right)\delta_{ij}$$
$$+ \frac{\partial}{\partial x_k}\left(\frac{\mu_{km}}{N_R}\frac{\partial R_{ij}}{\partial x_m}\right), \tag{11}$$

$$\overline{\rho} \frac{DL_t}{Dt} = C_{L1}\overline{\rho}\sqrt{2k} + C_{L2t}\overline{\rho}L_t\frac{\partial \widetilde{u}_i}{\partial x_i}$$
$$- C_{L3t}\overline{\rho}R_{ij}\frac{L_t}{k}\frac{\partial \widetilde{u}_i}{\partial x_j} + \frac{\partial}{\partial x_i}\left(\frac{\mu_{ij}}{N_{Lt}}\frac{\partial L_t}{\partial x_j}\right), \tag{12}$$

$$\overline{\rho} \frac{DL_d}{Dt} = C_{L1}\overline{\rho}\sqrt{2k} + C_{L2d}\overline{\rho}L_d\frac{\partial \widetilde{u}_i}{\partial x_i}$$
$$- C_{L3d}\overline{\rho}R_{ij}\frac{L_d}{k}\frac{\partial \widetilde{u}_i}{\partial x_j} + \frac{\partial}{\partial x_i}\left(\frac{\mu_{ij}}{N_{Ld}}\frac{\partial L_d}{\partial x_j}\right), \tag{13}$$

$$\overline{\rho} \frac{Da_j}{Dt} = a_j\frac{a_i}{2k}\frac{\partial \overline{p}}{\partial x_i} - C_A\overline{\rho}a_j\frac{\sqrt{2k}}{L_d} - R_{ij}\frac{\partial \overline{\rho}}{\partial x_i}$$
$$- C_{A2}\overline{\rho}a_i\frac{\partial \widetilde{u}_j}{\partial x_i} + \frac{\partial}{\partial x_i}\left(\frac{\mu_{ik}}{N_a}\frac{\partial a_j}{\partial x_k}\right), \tag{14}$$

$$\overline{\rho} \frac{D\mathcal{C}_{\alpha\beta}}{Dt} = C_{C1}\mu_{ij}\frac{\partial \widetilde{Y}_\alpha}{\partial x_i}\frac{\partial \widetilde{Y}_\beta}{\partial x_j} - C_{C2}\overline{\rho}\frac{\sqrt{2k}}{L_d}\mathcal{C}_{\alpha\beta}$$
$$+ C_{C3}\mathcal{C}_{\alpha\beta}\frac{a_i}{k}\frac{\partial \overline{p}}{\partial x_i} + \frac{\partial}{\partial x_i}\left(\frac{\mu_{ij}}{N_C}\frac{\partial \mathcal{C}_{\alpha\beta}}{\partial x_j}\right), \tag{15}$$

where

$$\frac{D}{Dt} \equiv \frac{\partial}{\partial t} + \widetilde{u}_i\frac{\partial}{\partial x_i}, \tag{16}$$

$$\mu_{ij} = \begin{cases} \overline{\rho}L_t\sqrt{R_{ij}}, & i = j \\ 0, & i \neq j \end{cases}, \tag{17}$$

and

$$k = \frac{1}{2}R_{ii}. \tag{18}$$

Since the mass fraction covariance matrix is symmetric, and mass fractions are constrained to sum to unity, only upper diagonal components need to be transported according to Eq. (15). So, for instance, in a problem involving three mixing components, only the $\mathcal{C}_{12}$, $\mathcal{C}_{13}$, and $\mathcal{C}_{23}$ components need to be transported. Remaining diagonal components of the mass fraction covariance matrix can be derived according to

$$\mathcal{C}_{\alpha\alpha} = \sum_{\beta=1,\beta\neq\alpha}^{N} -\mathcal{C}_{\alpha\beta}. \tag{19}$$

Note that Eq. (14) for transport of a_j has been written with the alternative buoyancy production term as described by Morgan [41] for the purpose of better capturing RT with gravity reversal. Additionally, the second production term involving C_{A2} has been included, as this term has been demonstrated important to prediction of transverse mass flux in the tilted rocket rig problem [49].

B. The R-ϕ-$2L$-a-$\mathcal{C}$ model

The R-ϕ-$2L$-a-$\mathcal{C}$ model is an RST extension of the k-ϕ-L-a-$\mathcal{C}$ model. It differs from the R-$2L$-a-$\mathcal{C}$ model primarily in its inclusion of an additional transport equation for the turbulence velocity ϕ, which allows the model to achieve high-order self-similar spatial profiles. Since ϕ is a characteristic velocity scale, it may not be possible to directly relate this quantity to something physically measurable from experiment. In interpreting the significance of ϕ, however, it is useful to consider how it is used in the model equations. The quantity $\frac{\phi}{L_d}$ defines the turbulent rate of destruction for all quantities except L_t. Therefore an alternative interpretation of ϕ is the dissipation rate of L_d. The transport length scale L_t, on the other hand, uses $\frac{k}{\phi}$ as a dissipation rate, and a similar quantity appears in the expression for μ_{ij}. Thus, while the velocity scale ϕ is primarily associated with destruction processes in this model, the related velocity scale $\frac{k}{\phi}$ is primarily associated with transport processes.

Notable differences from the k-ϕ-L-a-$\mathcal{C}$ model include the formulation of production terms in the ϕ equation and a_j equations. Where the original formulation of the k-ϕ-L-a-$\mathcal{C}$ model involved mass-fraction variance terms appearing in the denominators of several terms, by assuming a high-order spatial profile for ϕ in the R-ϕ-$2L$-a-$\mathcal{C}$ model, these terms have been reformulated to avoid such a construction, resulting in improved numerical stability. Note that the model transport equation for ϕ is not derived directly from the Navier-Stokes equations but is instead obtained heuristically by presupposing the existence of a turbulent destruction term, a turbulent diffusion term, and turbulent production terms due to buoyancy and shear effects. Additional model coefficients C_{p1}, C_{p2}, C_{p3}, N_R, N_R^*, and N_p are constrained through self-similarity analysis as described in Sec. III. Equations (20)–(29) summarize the R-ϕ-$2L$-a-$\mathcal{C}$ model:

$$\frac{D\overline{\rho}}{Dt} = -\overline{\rho}\frac{\partial\widetilde{u}_i}{\partial x_i}, \tag{20}$$

$$\overline{\rho}\frac{D\widetilde{Y}_\alpha}{Dt} = \frac{\partial}{\partial x_i}\left(\frac{\mu_{ij}}{N_Y}\frac{\partial\widetilde{Y}_\alpha}{\partial x_j}\right), \tag{21}$$

$$\overline{\rho}\frac{D\widetilde{u}_j}{Dt} = -\frac{\partial\overline{p}}{\partial x_j} - \frac{\partial}{\partial x_i}(\overline{\rho}R_{ij}) + \overline{\rho}g_j, \tag{22}$$

$$\overline{\rho}\frac{D\widetilde{e}}{Dt} = -\overline{p}\frac{\partial\widetilde{u}_i}{\partial x_i} - a_i\frac{\partial\overline{p}}{\partial x_i}$$
$$+ C_{R4}\overline{\rho}\frac{k\phi}{L_d} + \frac{\partial}{\partial x_i}\left(\frac{\mu_{ij}}{N_e}\frac{\partial\widetilde{e}}{\partial x_j}\right), \tag{23}$$

$$\overline{\rho}\frac{DR_{ij}}{Dt} = (1 - C_{R1})\hat{f}_{ij}\left(a_i\frac{\partial\overline{p}}{\partial x_j} + a_j\frac{\partial\overline{p}}{\partial x_i}\right)$$
$$+ (C_{R2} - 1)\overline{\rho}\hat{f}_{ij}\left(R_{ik}\frac{\partial\widetilde{u}_j}{\partial x_k} + R_{jk}\frac{\partial\widetilde{u}_i}{\partial x_k}\right)$$
$$- C_{R3}\overline{\rho}\frac{\phi}{L_d}\left(R_{ij} - \frac{1}{3}R_{kk}\delta_{ij}\right)$$
$$+ \frac{2}{3}\left(C_{R1}a_k\frac{\partial\overline{p}}{\partial x_k} - C_{R2}\overline{\rho}R_{mk}\frac{\partial\widetilde{u}_m}{\partial x_k} - C_{R4}\overline{\rho}\frac{k\phi}{L_d}\right)\delta_{ij}$$
$$+ \frac{\partial}{\partial x_k}\left(\frac{\mu_{km}}{\hat{N}_{R,ij}}\frac{\partial R_{ij}}{\partial x_m}\right), \tag{24}$$

$$\overline{\rho}\frac{D\phi}{Dt} = C_{p1}V^{3/8}\frac{a_i}{\phi}\frac{\partial\overline{p}}{\partial x_i} - C_{p2}\overline{\rho}\frac{\phi^2}{L_d}$$
$$- C_{p3}\overline{\rho}V^{3/16}\frac{R_{ij}}{\sqrt{k}}\frac{\partial\widetilde{u}_i}{\partial x_j} + \frac{\partial}{\partial x_i}\left(\frac{\mu_{ij}}{N_p}\frac{\partial\phi}{\partial x_j}\right), \tag{25}$$

$$\overline{\rho}\frac{DL_t}{Dt} = C_{L1}\overline{\rho}\frac{k}{\phi} + C_{L2t}\overline{\rho}L_t\frac{\partial\widetilde{u}_i}{\partial x_i}$$
$$- C_{L3t}\overline{\rho}R_{ij}\frac{L_t}{k}\frac{\partial\widetilde{u}_i}{\partial x_j} + \frac{\partial}{\partial x_i}\left(\frac{\mu_{ij}}{N_{Lt}}\frac{\partial L_t}{\partial x_j}\right), \tag{26}$$

$$\overline{\rho}\frac{DL_d}{Dt} = C_{L1}\overline{\rho}\phi + C_{L2d}\overline{\rho}L_d\frac{\partial\widetilde{u}_i}{\partial x_i}$$
$$- C_{L3d}\overline{\rho}R_{ij}\frac{L_d}{k}\frac{\partial\widetilde{u}_i}{\partial x_j} + \frac{\partial}{\partial x_i}\left(\frac{\mu_{ij}}{N_{Ld}}\frac{\partial L_d}{\partial x_j}\right), \tag{27}$$

$$\overline{\rho}\frac{Da_j}{Dt} = C_B a_j\frac{a_i}{k}\frac{\partial\overline{p}}{\partial x_i} - C_A\overline{\rho}a_j\frac{\phi}{L_d} - R_{ij}\frac{k}{\phi^2}\frac{\partial\overline{\rho}}{\partial x_i}$$
$$- C_{A2}\overline{\rho}a_i\frac{\partial\widetilde{u}_j}{\partial x_i} + \frac{\partial}{\partial x_i}\left(\frac{\mu_{ik}}{N_a}\frac{\partial a_j}{\partial x_k}\right), \tag{28}$$

$$\overline{\rho}\frac{D\mathcal{C}_{\alpha\beta}}{Dt} = C_{C1}\mu_{ij}\frac{\partial\widetilde{Y}_\alpha}{\partial x_i}\frac{\partial\widetilde{Y}_\beta}{\partial x_j} - C_{C2}\overline{\rho}\frac{\phi}{L_d}\mathcal{C}_{\alpha\beta}$$
$$+ C_{C3}\mathcal{C}_{\alpha\beta}\frac{a_i}{k}\frac{\partial\overline{p}}{\partial x_i} + \frac{\partial}{\partial x_i}\left(\frac{\mu_{ij}}{N_C}\frac{\partial\mathcal{C}_{\alpha\beta}}{\partial x_j}\right), \tag{29}$$

where

$$V = \sum_{\alpha=1}^{N-1}\sum_{\beta=\alpha+1}^{N} -\mathcal{C}_{\alpha\beta}, \tag{30}$$

$$\mu_{ij} = \overline{\rho}L_t\frac{R_{ij}}{\phi}, \tag{31}$$

$$k = \frac{1}{2}R_{ii}, \tag{32}$$

$$\hat{f}_{ij} = \begin{cases} \frac{k}{\phi^2}, & i \neq j \\ 1, & i = j \end{cases}, \tag{33}$$

and

$$\hat{N}_{R,ij} = \begin{cases} N_R^*, & i \neq j \\ N_R, & i = j \end{cases}. \tag{34}$$

The inclusion of $\hat{f}_{ij}$ and $\hat{N}_{R,ij}$ in Eq. (24) introduce differing self-similar spatial profiles for the Reynolds normal stresses compared to the Reynolds shear stresses. As described in the next section, this inclusion is necessary to achieve high-order self-similar spatial profiles for 1D RT and KH test problems.

III. SELF-SIMILARITY OF THE R-ϕ-$2L$-a-$\mathcal{C}$ MODEL

A. Self-similarity of an RT mixing layer

To begin, a change of variable is introduced in terms of the mixing layer half-width $h(t)$ such that $\chi \equiv x/h$. The similarity ansatz is then assumed such that the scalar heavy mass fraction profile across the mixing layer is given by

$$Y_H(\chi) = \frac{1}{A_Y} \int_{-1}^{\chi} (1 - \hat{\chi}^2)^{n_Y} d\hat{\chi}, \tag{35}$$

where n_Y is an arbitrary exponent, and A is a normalization constant given in terms of the gamma function Γ by

$$A_Y = \sqrt{\pi} \frac{\Gamma(n_Y + 1)}{\Gamma(n_Y + \frac{3}{2})}. \tag{36}$$

It is assumed that the turbulence variables R_{xx}, ϕ, L_t, L_d, a, and $\mathcal{C}_{\alpha\beta}$ are separable in space and time:

$$R_{xx}(\chi, t) = R_0(t) f^{n_k}(\chi), \tag{37a}$$

$$\phi(\chi, t) = P_0(t) f^{n_k - 1/2}(\chi), \tag{37b}$$

$$L_t(\chi, t) = L_{t0}(t) f^{1/2}(\chi), \tag{37c}$$

$$L_d(\chi, t) = L_{d0}(t) f^{n_k - 1/2}(\chi), \tag{37d}$$

$$a(\chi, t) = A_0(t) f^{n_k}(\chi), \tag{37e}$$

$$\mathcal{C}_{\alpha\beta}(\chi, t) = -V_0(t) f^{2n_Y + 1}(\chi), \tag{37f}$$

where the spatial function $f(\chi) \equiv 1 - \chi^2$. The Reynolds stress components R_{xx} and $R_{yy} = R_{zz}$ are related through the RT anisotropy tensor,

$$B_{ij}^{RT} = \frac{R_{ij} - \frac{2}{3} k \delta_{ij}}{2k} = \frac{R_{ij}}{R_{xx} + 2R_{yy}} - \frac{1}{3} \delta_{ij}. \tag{38}$$

It thus follows for a 1D self-similar RT mixing layer,

$$R_{yy} = R_{xx} \left(\frac{\frac{1}{3} - \frac{B_{xx}^{RT}}{2}}{\frac{1}{3} + B_{xx}^{RT}} \right). \tag{39}$$

The general approach to using self-similarity analysis has been described previously for the k-L [20,28], k-L-a [26], k-$2L$-a [29], k-L-a-$\mathcal{C}$ [30,37,40], and k-ϕ-L-a-$\mathcal{C}$ [38,40] models. Given the parallels of the current approach to what has been previously published, many of the details will not be reproduced here, and only key results are presented. Generally speaking, the self-similarity procedure proceeds by substituting Eqs. (35) and (37) into the turbulence Eqs. (24)–(29). Reduced turbulence equations are then obtained which can be written as a second-moment component proportional to χ^2 and a zero-moment component. The separability ansatz represented by Eqs. (37) requires that both components must

simultaneously go to zero, which provides the following constraints on diffusion coefficients:

$$N_a = N_R = N_e = N_Y = 2n_k N_{Lt}, \tag{40a}$$

$$N_{Ld} = N_p = (2n_k - 1) N_{Lt}, \tag{40b}$$

$$N_C = 2(2n_Y + 1) N_{Lt}. \tag{40c}$$

To relate the turbulence length scale to the mixing layer half-width, it is assumed $L_{t0} = \beta h$. From the reduced form of Eq. (26), satisfaction of the separability ansatz requires

$$\beta = \sqrt{\frac{C_{L1} N_{Lt}}{4C_\mu \left(\frac{1}{3} + B_{xx}^{RT} \right)}}. \tag{41}$$

From the reduced Eq. (27), it is then possible to solve

$$\frac{L_{t0}}{L_{d0}} = \frac{1}{2 \left(\frac{1}{3} + B_{xx}^{RT} \right)} \frac{R_0}{P_0^2}. \tag{42}$$

Note that Eq. (42) implies that the ratio of L_t / L_d will be constant if the ratio k/ϕ^2 is also constant. Simultaneous satisfaction of the reduced Eq. (24) for both R_{xx} and R_{yy} requires

$$C_{R4} = C_{R3} \tag{43}$$

and

$$B_{xx}^{RT} = \frac{2}{3}(1 - C_{R1}). \tag{44}$$

Then, by imposing constraints that $\frac{\partial}{\partial t} \left(\frac{P_0}{A_0} \right) = 0$ and $\frac{\partial}{\partial t} \left(\frac{R_0}{P_0^2} \right) = 0$, from the reduced Eqs. (28) and (25), the following two constraints must be satisfied:

$$C_B = \frac{4 \frac{C_{p2}}{C_{L1}} + 3}{4 \left(1 + \frac{C_{R3}}{C_{L1}} \right)} \tag{45}$$

and

$$\frac{C_A}{C_{L1}} = \frac{1}{8A_Y \alpha_b \left(1 + \frac{C_{R3}}{C_{L1}} \right)} \frac{R_0}{P_0^2} + \frac{C_{p2}}{C_{L1}}. \tag{46}$$

In Eq. (46) α_b is the RT growth parameter such that the mixing layer is assumed to grow proportional to α_b and the conventional Atwood number A_T according to $h = \alpha_b A_T g t^2$. Note that this definition of α_b is an algebraic relationship expected to be valid in the self-similar limit under consideration. Other differential relationships such as the one by Ristrocelli and Clark [50] could instead be used that can accommodate linear and constant contributions to the mixing layer growth. In the limit of self-similarity, however, these contributions become vanishingly small and only the quadratic contribution remains. For additional discussion of alternative ways to define α_b, the reader is referred to works by Banerjee *et al.* [51] and Schilling [10]. The ratio $\frac{R_0}{P_0^2}$ is then solved according to

$$\frac{R_0}{P_0^2} = \frac{\left(\frac{1}{3} + B_{xx}^{RT} \right) \left(4 \frac{C_{p2}}{C_{L1}} + 3 \right)}{2C_{p1} \left(1 + \frac{C_{R3}}{C_{L1}} \right)} V_0^{\frac{1 - n_k}{2n_Y + 1}}. \tag{47}$$

The RT mixedness parameter is defined by

$$\Theta_{RT} \equiv 1 + \frac{\int_{-1}^{1} \widetilde{Y_H'' Y_L''} \, d\chi}{\int_{-1}^{1} \widetilde{Y}_H \widetilde{Y}_L \, d\chi} = 1 + \frac{\int_{-1}^{1} \mathcal{C}_{HL} \, d\chi}{\int_{-1}^{1} \widetilde{Y}_H \widetilde{Y}_L \, d\chi}. \tag{48}$$

To simplify Eq. (48), recognize for $n_Y = 3/2$,

$$V_0 \int_{-1}^{1} (1 - \chi^2)^{2n_Y + 1} d\chi = V_0 \frac{256}{315} \qquad (49)$$

and

$$\int_{-1}^{1} \overline{Y}_H \overline{Y}_L \, d\chi = \int_{-1}^{1} \left[\frac{1}{A_Y} \int_{-1}^{\chi} (1 - \hat{\chi}^2)^{n_Y} d\hat{\chi} \right]$$
$$\times \left[1 - \frac{1}{A_Y} \int_{-1}^{\chi} (1 - \hat{\chi}^2)^{n_Y} d\hat{\chi} \right] d\chi$$
$$\approx 0.234. \qquad (50)$$

Substituting Eqs. (49) and (50) back into Eq. (48) and rearranging to solve for V_0 gives

$$V_0 \approx 0.288(1 - \Theta_{RT}). \qquad (51)$$

Recalling from Eq. (47) that C_{p1} can be used to fix the ratio $\frac{R_0}{P_0^2}$, for consistency with the R-$2L$-a-$\mathcal{C}$ model, we choose

$$C_{p1} = V_0^{\frac{1}{2n_Y + 1}}. \qquad (52)$$

Then, utilizing the reduced Eq. (29) and recognizing $\dot{V}_0 = 0$ gives the following constraint on C_{C3}:

$$C_{C3} = \frac{2\frac{C_{c2}}{C_{L1}} + 1}{2\left(1 + \frac{C_{R3}}{C_{L1}}\right)} - \frac{C_{C1}N_{Lt}}{2A_Y^2 V_0\left(1 + \frac{C_{R3}}{C_{L1}}\right)}. \qquad (53)$$

Finally, to obtain a constraint on N_{Lt}, the energy balance within an RT mixing layer is considered. The turbulent kinetic energy generated within an RT mixing layer is be given by

$$E_K = \int_{-h}^{h} \overline{\rho} k(x, t) \, dx \approx \frac{\rho_0}{2} \frac{R_0}{\frac{1}{3} + B_{xx}^{RT}} A_k h, \qquad (54)$$

where A_k is the normalization constant,

$$A_k = \sqrt{\pi} \frac{\Gamma(n_k + 1)}{\Gamma\left(n_k + \frac{3}{2}\right)}. \qquad (55)$$

The gravitational potential energy within the RT mixing layer is derived by imagining a material interface at $x = 0$ and integrating over a distance $2d$,

$$\text{PE} = -g \int_{-d}^{d} \overline{\rho}(x) x \, dx. \qquad (56)$$

Evaluating Eq. (56) and considering only the difference over the mixing width $-h \leqslant x \leqslant h$ gives the change in potential energy over the mixing layer as

$$\Delta \text{PE} = \left(1 - \frac{2n_Y + 2}{2n_Y + 3}\right) A_T g \rho_0 h^2. \qquad (57)$$

Thus, the fraction of potential energy converted to kinetic energy can be expressed:

$$\frac{E_K}{\Delta \text{PE}} = \frac{16 A_k \alpha_b C_{p1} N_{Lt} \left(1 + \frac{C_{R3}}{C_{L1}}\right) V_0^{\frac{n_k - 1}{2n_Y + 1}}}{C_{L1} C_\mu \left(1 - \frac{2n_Y + 2}{2n_Y + 3}\right)\left(4\frac{C_{p2}}{C_{L1}} + 3\right)\left(\frac{1}{3} + B_{xx}^{RT}\right)}. \qquad (58)$$

B. Self-similarity of a KH mixing layer

To obtain constraints on shear production terms in Eqs. (24) through (29), the case of a quasi-1D shear layer is

considered. In this case, $\widetilde{u}_x$ is a function of a single spatial dimension, y, and $\widetilde{u}_y = 0$. In terms of the similarity variable, $\chi = y/h(t)$,

$$\widetilde{u}_x(\chi) = \begin{cases} U_2, & \chi \geqslant 1 \\ U_c[1 - \mathcal{A} + 2\mathcal{A}v_2(\chi)], & -1 < \chi < 1 \\ U_1, & \chi \leqslant -1, \end{cases} \qquad (59)$$

where

$$v_2(\chi) = \frac{1}{A_u} \int_{-1}^{\chi} (1 - \hat{\chi}^2)^{n_u} d\hat{\chi} \qquad (60)$$

and

$$A_u = \sqrt{\pi} \frac{\Gamma(n_u + 1)}{\Gamma\left(n_u + \frac{3}{2}\right)}. \qquad (61)$$

The convective velocity is then defined as

$$U_c = \frac{U_2 + U_1}{2}, \qquad (62)$$

and $\mathcal{A}$ is the Kelvin-Helmholtz Atwood number defined by

$$\mathcal{A} = \frac{U_2 - U_1}{U_2 + U_1}. \qquad (63)$$

To relate the shear stress to the normal stresses, the shear correlation coefficient is defined as

$$\mathcal{S}_{xy} \equiv -\frac{R_{xy}}{\sqrt{R_{xx}}\sqrt{R_{yy}}} = -\frac{R_{xy}}{R_{xx}} \sqrt{\frac{\frac{1}{3} + B_{xx}^{KH}}{\frac{1}{3} - \frac{B_{xx}^{KH}}{2}}}, \qquad (64)$$

where B_{xx}^{KH} is the anisotropy of a KH mixing layer, as defined analogously to the RT anisotropy given by Eq. (38). Following a similar approach as before, it is assumed that L_{t0} is proportional to h such that $L_{t0} = \beta h$. By assuming $n_u = \frac{n_Y}{2}$ and $R_{xy} = R_0 f^{n_u + 1}$, then satisfaction of the separability ansatz in the reduced L_t equation requires

$$\beta^2 - \frac{C_{L3t} N_{Lt}}{A_u C_\mu} \mathcal{S}_{xy} \sqrt{\frac{\left(\frac{1}{3} + B_{xx}^{KH}\right)^3}{\frac{1}{3} - \frac{B_{xx}^{KH}}{2}}} \frac{P_0^2}{R_0} \frac{\Delta U}{P_0} \beta$$
$$- \frac{C_{L1} N_{Lt}}{4 C_\mu \left(\frac{1}{3} - \frac{B_{xx}^{KH}}{2}\right)} = 0. \qquad (65)$$

Satisfaction of the separability ansatz within the reduced R_{xy} equation requires

$$N_R^* = (n_Y + 2) N_{Lt}. \qquad (66)$$

Then, as with the RT problem, simultaneous satisfaction of the reduced R_{xy}, R_{xx}, and R_{yy} equations requires

$$B_{xx}^{KH} = \frac{2}{3}(1 - C_{R2}) \qquad (67)$$

and

$$\mathcal{S}_{xy}^2 = \frac{3 B_{xx}^{KH}}{8\left(\frac{1}{3} + B_{xx}^{KH}\right)^2} \frac{R_0}{P_0^2}. \qquad (68)$$

Equation (68) is then utilized in conjunction with the reduced L_d equation to obtain

$$\frac{\sqrt{R_0}}{P_0} = \frac{\left(2\frac{C_{p2}}{C_{L1}} + 1\right) + C_{L3d}\left(\frac{C_{R3}}{C_{L1}} - \frac{C_{p2}}{C_{L1}}\right)}{\left(\frac{C_{R3}}{C_{L1}} + \frac{1}{2}\right)C_{p3}V_0^{3/16}\sqrt{2\left(\frac{1}{3} + B_{xx}^{KH}\right)}}\left(\frac{1}{3} + B_{xx}^{KH}\right).$$

(69)

In Eq. (69) V_0 is given in terms of the KH mixedness Θ_{KH} in a manner analogous to Eqs. (48) through (51),

$$V_0 \approx 0.288(1 - \Theta_{KH}).$$

(70)

Equation (69) is then used in the reduced ϕ equation, along with the constraint that $\frac{\partial}{\partial t}\left(\frac{R_0}{P_0^2}\right) = 0$ to solve

$$\frac{R_0}{\Delta U^2} = \frac{1 + C_{L3d}\frac{C_{R3}}{C_{L1}}}{\left(\frac{C_{R3}}{C_{L1}} + \frac{1}{2}\right)A_u^2(n_Y + 2)}\left(\frac{1}{3} + B_{xx}^{KH}\right).$$

(71)

It is additionally useful to use Eq. (38) to relate $\frac{R_0}{\Delta U^2}$ to the peak TKE according to

$$\frac{K_0}{\Delta U^2} = \frac{R_0}{\Delta U^2}\left(\frac{1}{\frac{2}{3} + 2B_{xx}^{KH}}\right).$$

(72)

As Sec. III C will show, the coefficient ratios $\frac{C_{R3}}{C_{L1}}$ and $\frac{C_{p2}}{C_{L1}}$ are both constrained by the decay of homogeneous isotropic turbulence. Thus, Eqs. (68) through (71) demonstrate that if $\frac{R_0}{\Delta U^2}$ is determined by C_{L3d}, then $\frac{R_0}{P_0^2}$ (and by extension $\mathcal{S}_{xy}$) must be determined by C_{p3}. Consider, however, that for a spatially evolving shear layer, the nondimensional growth rate δ is defined as

$$\delta \equiv \frac{dh}{dx}.$$

(73)

It is therefore possible to write for the temporally evolving shear layer

$$\dot{h} = \frac{dh}{dx}\frac{dx}{dt} = \delta U_c.$$

(74)

Utilizing $L_{t0} = \beta h$ with the reduced L_t equation then gives the following expression for the KH growth parameter:

$$\frac{\delta}{\mathcal{A}} = 2A_u(n_Y + 2)\mathcal{S}_{xy}\frac{R_0}{\Delta U^2}\sqrt{\frac{\frac{1}{3} - \frac{B_{xx}^{KH}}{2}}{\frac{1}{3} + B_{xx}^{KH}}}.$$

(75)

An unfortunate degeneracy of constraints therefore exists that implies if $\mathcal{S}_{xy}$, $\frac{R_0}{\Delta U^2}$, and B_{xx}^{KH} are already determined by the coefficients C_{p3}, C_{L3d}, and C_{R2}, respectively, then the growth parameter δ cannot be set independently. It is worth noting that no such constraint degeneracies exist in the k-$2L$-a-$\mathcal{C}$ and k-ϕ-L-a-$\mathcal{C}$ models. As will be shown in Sec. IV, however, it fortunately works out that satisfactory calibration for all three nondimensional parameters can be achieved with the R-$2L$-a-$\mathcal{C}$ and R-ϕ-$2L$-a-$\mathcal{C}$ models, even with the noted constraint degeneracies.

Substitution into Eq. (29) and applying Eq. (40c) then results in the reduced V_0 equation, which is rearranged to obtain

$$C_{C1} = A_Y^2V_0\left[\frac{C_{C2}}{C_\mu\beta^2}\left(\frac{\frac{1}{3} + B_{xx}^{KH}}{\frac{1}{3} - \frac{B_{xx}^{KH}}{2}}\right)\frac{L_{t0}}{L_{d0}}\frac{P_0^2}{R_0} + \frac{1}{N_{Lt}}\right],$$

(76)

where the ratio $\frac{L_{t0}}{L_{d0}}$ is solved from the reduced L_d equation according to

$$\frac{L_{t0}}{L_{d0}} = \frac{2C_\mu}{N_{Lt}C_{L1}}\beta^2\frac{R_0}{P_0^2}\left(\frac{\frac{1}{3} - \frac{B_{xx}^{KH}}{2}}{\frac{1}{3} + B_{xx}^{KH}}\right)$$

$$- \frac{2\left(\frac{1}{3} + B_{xx}^{KH}\right)C_{L3d}}{A_uC_{L1}}\mathcal{S}_{xy}\sqrt{\frac{\frac{1}{3} - \frac{B_{xx}^{KH}}{2}}{\frac{1}{3} + B_{xx}^{KH}}}\beta\frac{\Delta U}{P_0}.$$

(77)

Finally, solving quadratic Eq. (65) for β and substituting into Eq. (22) then leads to the following constraint for C_{L3t}:

$$C_{L3t} = \frac{A_u^2(n_Y + 2)}{\left(\frac{1}{3} + B_{xx}^{KH}\right)}\frac{R_0}{\Delta U^2}$$

$$- \frac{C_{L1}C_\mu}{4N_{Lt}(n_Y + 2)\mathcal{S}_{xy}^2\left(\frac{1}{3} + B_{xx}^{KH}\right)^2}\frac{R_0}{P_0^2}.$$

(78)

C. Decaying homogeneous isotropic turbulence

In the absence of mean velocity or pressure gradients, the model equations reduce to

$$\frac{dk}{dt} = -C_{R3}\frac{k\phi}{L_d},$$

(79)

$$\frac{dL_d}{dt} = C_{L1}\phi,$$

(80)

$$\frac{d\phi}{dt} = -C_{p2}\frac{\phi^2}{L_d},$$

(81)

$$\frac{dC_{\alpha\beta}}{dt} = -C_{C2}\frac{C_{\alpha\beta}\phi}{L_d}.$$

(82)

These equations are solved in terms of a reference time, t_0, and decay exponents, n and m:

$$k = K_0\left(1 + \frac{t}{t_0}\right)^{-n},$$

(83a)

$$L_d = L_{d0}\left(1 + \frac{t}{t_0}\right)^{1-n/2},$$

(83b)

$$\phi = P_0\left(1 + \frac{t}{t_0}\right)^{-n/2},$$

(83c)

$$C_{\alpha\beta} = V_0\left(1 + \frac{t}{t_0}\right)^{-m}.$$

(83d)

Substituting Eqs. (83a) through (83d) back into Eqs. (79) through (82) leads to the following constraints after some algebra:

$$\frac{C_{R3}}{C_{L1}} = \frac{2n}{2 - n},$$

(84)

$$\frac{C_{p2}}{C_{L1}} = \frac{n}{n - 2},$$

(85)

$$\frac{C_{C2}}{C_{L1}} = \frac{2m}{2 - n}.$$

(86)

D. Summary of constraints

Equations (40), (43), (44), (45), (46), (52), (53), (58), (66), (67), (71), (75), (76), (78), and (84) through (86) thus represent 23 constraints on the 23 model coefficients C_{R1}, C_{R2}, C_{R4}, C_{L1},

$C_{L3t}, C_{L3d}, C_A, C_{C1}, C_{C2}, C_{C3}, C_{p1}, C_{p2}, C_{p3}, N_R, N_R^*, N_p, N_e, N_Y,$ $N_R, N_{Lt}, N_{Ld}, N_a,$ and N_C in terms of the 10 self-similar growth parameters $B_{xx}^{RT}, \alpha_b, \Theta_{RT}, \frac{E_K}{\Delta PE}, B_{xx}^{KH}, \Theta_{KH}, \frac{K_0}{\Delta U^2}, \frac{\delta}{\mathcal{A}}, n,$ and m. Coefficients C_{L2t} and C_{L2d} are constrained to ensure the total velocity divergence contribution to the L_t and L_d equations is 1/3 [20,31],

$$C_{L2t} = \tfrac{1}{3} + \tfrac{2}{3}C_{L3t}, \tag{87a}$$

$$C_{L2d} = \tfrac{1}{3} + \tfrac{2}{3}C_{L3d}. \tag{87b}$$

Coefficient C_{A2} is not constrained through similarity analysis because the term it modifies in the a equation drops out of the reduced a equation for 1D RT. As discussed later in Sec. IV C, however, this term is important to the transverse mass flux in the tilted rocket rig problem [49]. It is therefore anticipated that $C_{A2} \approx 1$. Coefficients C_μ and one of either C_{L1} or C_{R3} end up being free parameters that do not affect the realized self-similar behavior if the constraints above are satisfied. Thus, for simplicity we take $C_\mu = C_{R3} = 1$. The shape exponents n_k and n_u are constrained such that $n_k = n_Y + 1$, and $n_u = \frac{n_Y}{2}$. A good fit to high-fidelity simulation data is found for $n_Y = \frac{3}{2}$ [38]. Table I summarizes a nominal set of model coefficients and growth parameters that will be used for simulations in Sec. IV. Growth parameters for RT mixing are chosen to be generally consistent with direct numerical simulation by Cabot and Cook [52] and with LES by Morgan *et al.* [53]. Kelvin-Helmholtz growth parameters are chosen to be consistent with experimental data from Bell and Mehta [54] as well as LES by Morgan [37]. The mechanical turbulence decay exponent n is chosen to be more or less consistent with measurements by Batchelor and Townsend [55]. This parameter has been previously shown to be degenerate with the RM growth exponent [20,26], and a choice of $n = 1.111$ corresponds to an RM growth exponent of 0.25, which is generally consistent with experimental observations by Dimonte and Schneider [56]. Finally, the scalar decay exponent m is chosen by relation to n through the relationship $m = \frac{1}{2}(6 - 3n)$, as suggested by Sutton [57].

IV. NUMERICAL RESULTS

The R-2L-a-$\mathcal{C}$ and R-ϕ-2L-a-$\mathcal{C}$ models have been implemented in the RANSBOX library [58], and simulation results in this section are computed using the ARES code [28], which is a second-order arbitrary Lagrangian/Eulerian hydrodynamics code that integrates RANSBOX for RANS model evaluation.

A. 1D Rayleigh-Taylor mixing layer

We first consider a 1D hydrostatic RT mixing layer between two ideal, monatomic gases subject to constant acceleration at Atwood number $A_T = 0.05$. This problem is set up in a domain of size 1 cm with 1600 uniformly spaced computational zones. Turbulence length scales are initialized to zero everywhere except for the two zones bordering the interface at $y = 0$, where $L_t = L_d = \lambda_0 = 4.0 \times 10^{-6}$ cm. Reynolds stresses are initialized to zero everywhere except the two interface zones such that k is initialized to $1.0\,\mathrm{cm}^2/\mathrm{s}^2$ in these zones. For the R-ϕ-2L-a-$\mathcal{C}$ model, ϕ is initialized to $\sqrt{k}$.

TABLE I. Nominal R-ϕ-2L-a-$\mathcal{C}$ model coefficients and the self-similarity parameters that constrain them.

Growth parameter	Value
B_{xx}^{RT}	0.300
α_b	0.025
Θ_{RT}	0.800
$\frac{E_K}{\Delta PE}$	0.500
B_{xx}^{KH}	0.123
Θ_{KH}	0.800
$\frac{K_0}{\Delta U^2}$	0.033
$\frac{\delta}{\mathcal{A}}$	0.080
n	1.111
m	1.333
Shape parameter	**Value**
n_Y	1.500
n_k	2.500
n_u	0.750
Model coefficient	**Value**
C_μ	1.000
C_{R1}	0.550
C_{R2}	0.815
C_{R3}, C_{R4}	1.000
C_B	0.354
C_{L1}	0.400
C_{L2t}	0.088
C_{L3t}	−0.368
C_{L2d}	0.449
C_{L3d}	0.173
C_{p1}	0.490
C_{p2}	0.500
C_{p3}	1.392
C_A	2.589
C_{A2}	1.000
C_{C1}	0.528
C_{C2}	1.200
C_{C3}	0.311
N_a, N_R, N_e, N_Y	3.656
N_{Ld}, N_p	2.925
N_C	5.849
N_R^*	2.559
N_{Lt}	0.731

In Fig. 1 the realized RT growth parameter $\alpha_b = h/(A_T g t^2)$, mixedness parameter Θ_{RT}, and anisotropy parameter B_{xx}^{RT} are plotted against nondimensional time (where $t_0 = \sqrt{\lambda_0/(A_T g)}$) for simulations using both the R-2L-a-$\mathcal{C}$ and the R-ϕ-2L-a-$\mathcal{C}$ models. Figure 1(a) illustrates that both models asymptote to the anticipated value of $\alpha_b = 0.025$, which was used to constrain the model coefficients. High-frequency oscillations appearing in this figure are numerical artifacts resulting from trapped acoustic modes generated as a result of the sharp initial conditions. Similarly, Figs. 1(b)
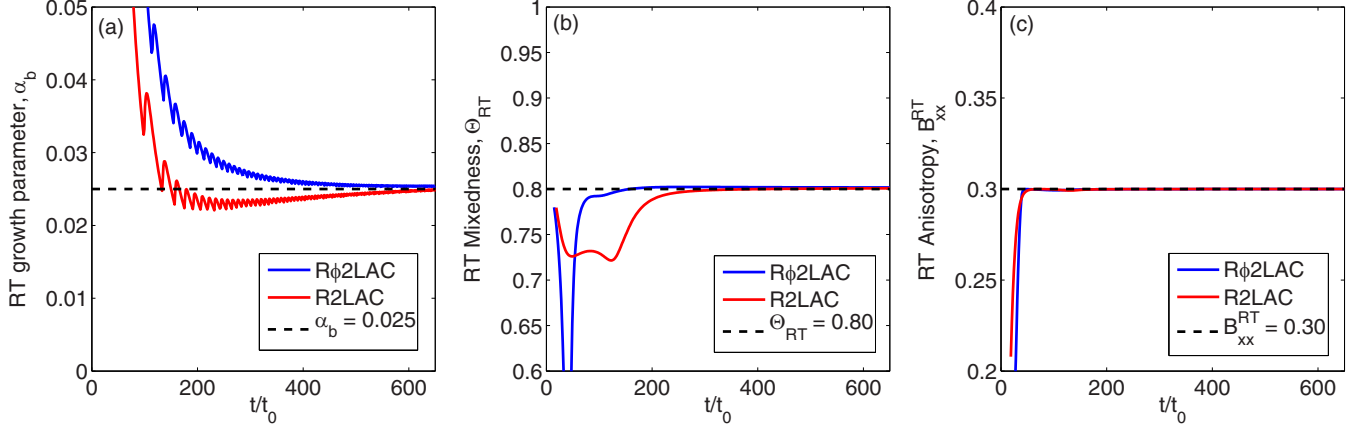
FIG. 1. Time evolution of three RT self-similarity parameters with both the R-2L-a-$\mathcal{C}$ and the R-ϕ-2L-a-$\mathcal{C}$ models: (a) the RT growth parameter $\alpha_b = h/(A_T g t^2)$, (b) the RT mixedness parameter Θ_{RT}, and (c) the RT anisotropy parameter B_{xx}^{RT}.

and 1(c) illustrate that the mixedness and anisotropy realized in the simulations rapidly approach the anticipated values of $\Theta_{RT} = 0.80$ and $B_{xx}^{RT} = 0.30$. These results serve to validate the similarity analyses presented previously in Sec. III and in Appendix by demonstrating that the anticipated self-similarity parameters are indeed recovered.

Figure 2 demonstrates the main difference between the R-2L-a-$\mathcal{C}$ and the R-ϕ-2L-a-$\mathcal{C}$ models by plotting steady-state spatial profiles of average mass fraction $\widetilde{Y}_H$, normalized Reynolds stresses $\frac{R_{ij}}{K_0}$ (where K_0 is the peak TKE), and the heavy mass fraction covariance $C_{HH} = \widetilde{Y_H'' Y_H''}$. RANS results in Fig. 2 are additionally compared against large-eddy simulation (LES) data from Morgan *et al.* [53]. While the R-2L-a-$\mathcal{C}$ results provide a reasonable approximation to the LES, it is clear that the high-order spatial profiles of the R-ϕ-2L-a-$\mathcal{C}$ model are in better agreement, particularly in the tails. Both RANS models, however, capture the relative magnitude of the Reynolds stresses in Fig. 2(b), which indicates the calibration value of B_{xx}^{RT} matches LES well. Comparison of the heavy mass fraction variance similarly indicates that the calibration value of $\Theta_{RT} = 0.80$ provides good agreement with LES, despite minor overprediction in the peak in

Fig. 2(c). Given the close agreement between the R-ϕ-2L-a-$\mathcal{C}$ model and LES in the spatial profile of $\widetilde{Y}_H$, it is likely that mixedness of the LES data in Fig. 2(c) is slightly greater than 0.80.

B. Quasi-1D Kelvin-Helmholtz mixing layer

Next, we consider KH mixing layer simulations run with 960 uniformly spaced computational zones on a domain extending from $y = -48.0$ cm to $y = 48.0$ cm. Turbulence length scales are initialized to zero everywhere except for the two zones bordering the interface at $y = 0$, where $L_t = L_d = \lambda_0 = 0.44$ cm. Reynolds stresses are initialized to zero everywhere except for the two interface zones such that k is initialized to $0.01(\Delta U)^2$ in these zones, and as before for the R-ϕ-2L-a-$\mathcal{C}$ model, ϕ is initialized to $\sqrt{k}$. The initial velocity profile is chosen to match the Bell and Mehta experiment [54] such that $\widetilde{u}_x = U_1 = 900$ cm/s for $y < 0$ and $\widetilde{u}_x = U_2 = 1500$ cm/s for $y \geqslant 0$, corresponding to $\mathcal{A} = 0.25$.

In Fig. 3 the normalized TKE magnitude $\frac{K_0}{\Delta U^2}$, mixedness parameter Θ_{KH}, and anisotropy parameter B_{xx}^{KH} are plotted against nondimensional time (where $t_0 = \lambda_0/\Delta U$) for
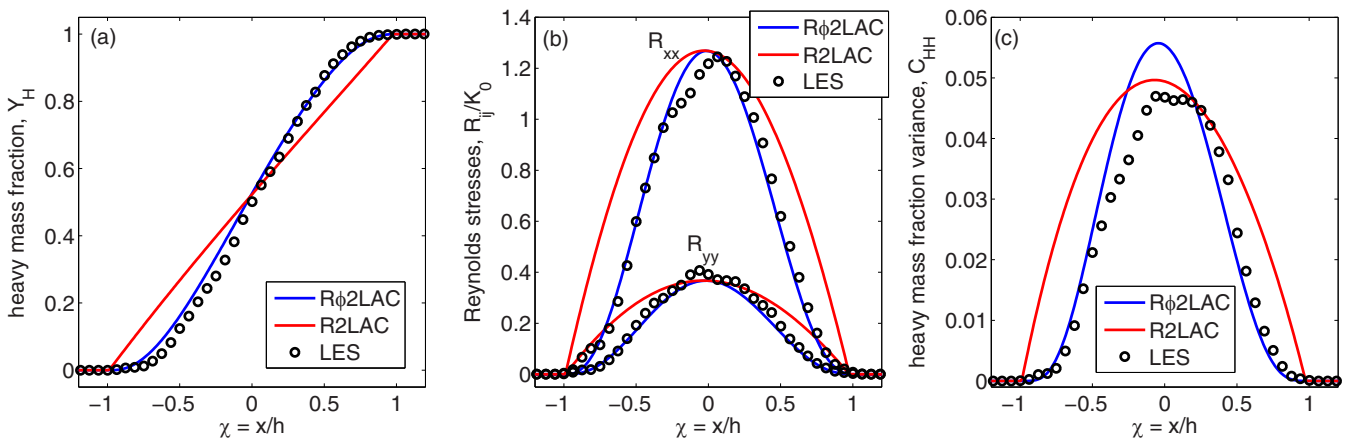
FIG. 2. Comparison of RT spatial profiles between the R-2L-a-$\mathcal{C}$ model, the R-ϕ-2L-a-$\mathcal{C}$ model, and LES by Morgan *et al.* [53]: (a) average mass fraction of the heavy species, $\widetilde{Y}_H$, (b) normalized Reynolds stresses, R_{ij}/K_0, and (c) heavy mass fraction variance $C_{HH} = \widetilde{Y_H'' Y_H''}$ are all plotted vs the spatial similarity variable $\chi = x/h$.
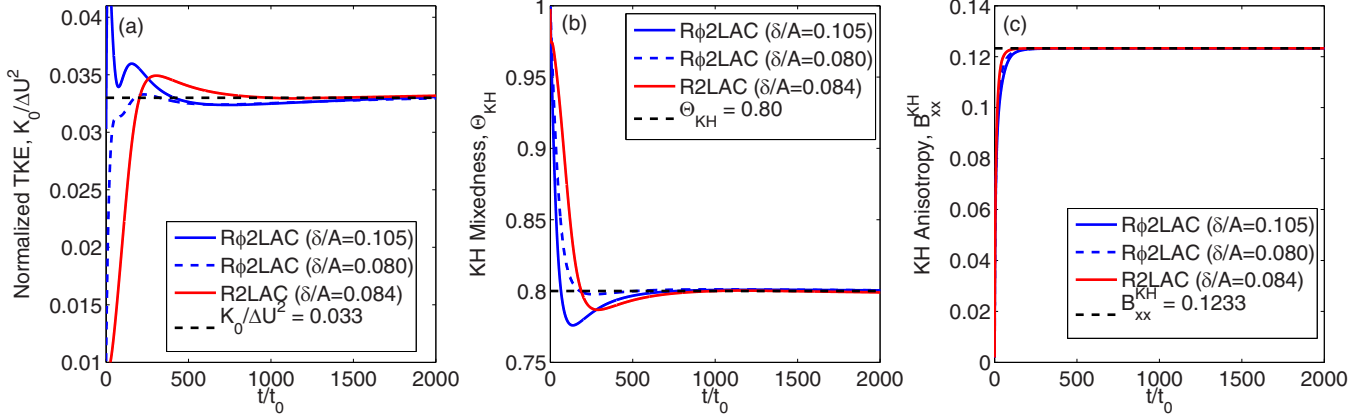
FIG. 3. Time evolution of three KH self-similarity parameters with both the R-$2L$-a-$\mathcal{C}$ and the R-ϕ-$2L$-a-$\mathcal{C}$ models: (a) normalized peak TKE $\frac{K_0}{\Delta U^2}$ (b) the KH mixedness parameter Θ_{KH}, and (c) the KH anisotropy parameter B_{xx}^{KH}. Two different simulations with the R-ϕ-$2L$-a-$\mathcal{C}$ models are shown, where model coefficients have been constrained for $\frac{\delta}{\mathcal{A}} = 0.080$ (solid blue) and for $\frac{\delta}{\mathcal{A}} = 0.105$ (dashed blue).

simulations using both the R-$2L$-a-$\mathcal{C}$ and the R-ϕ-$2L$-a-$\mathcal{C}$ models. Recall from Sec. III that a constraint degeneracy was identified such that only two of B_{xx}^{KH}, $\frac{\delta}{\mathcal{A}}$, and $\mathcal{S}_{xy}$ can be independently calibrated with the R-ϕ-$2L$-a-$\mathcal{C}$ model. For this reason, in Fig. 3 results from two different simulations with the R-ϕ-$2L$-a-$\mathcal{C}$ model are presented. In both sets of results anisotropy is held fixed at $B_{xx}^{KH} = 0.1233$; in one set, a choice is made to calibrate $\frac{\delta}{\mathcal{A}} = 0.080$ (which results in $\mathcal{S}_{xy} = 0.342$), while in the other set of results, the choice is made to calibrate $\mathcal{S}_{xy} = 0.45$ (which results in $\frac{\delta}{\mathcal{A}} = 0.105$). As discussed in Appendix, for the R-$2L$-a-$\mathcal{C}$ model only one of B_{xx}^{KH}, $\frac{\delta}{\mathcal{A}}$, or $\mathcal{S}_{xy}$ can be independently calibrated. Thus, for R-$2L$-a-$\mathcal{C}$ results, B_{xx}^{KH} is set to 0.1233, which fortuitously results in $\mathcal{S}_{xy} = 0.45$ and $\frac{\delta}{\mathcal{A}} = 0.084$. Results in Figs. 3(a) through 3(c) indicate that all three self-similarity parameters rapidly approach their expected asymptotic values for all three sets of results presented, providing further confidence in the accuracy of the self-similarity analyses in Sec. III and Appendix.

Figure 4 illustrates how calibration of $\mathcal{S}_{xy}$ and $\frac{\delta}{\mathcal{A}}$ is linked by plotting as a function of nondimensional time the mixing

layer width, the realized growth parameter $\frac{\delta}{\mathcal{A}}$, and the realized shear stress correlation $\mathcal{S}_{xy}$. As seen in Figs. 4(a) and 4(b), the realized mixing layer growth rate is slightly different among the three simulations, despite all achieving the same level of anisotropy and TKE magnitude. In all three simulations, the expected asymptotic growth rate is achieved by about $t/t_0 = 500$. The expected asymptotic shear stress correlation is achieved similarly rapidly for all three simulations. What is particularly notable is that from experiment such as the one by Bell and Mehta [54], it is expected that $\frac{\delta}{\mathcal{A}} \approx 0.08$ and $\mathcal{S}_{xy} \approx 0.45$. In this regard, it is somewhat surprising that the R-$2L$-a-$\mathcal{C}$ model is able to achieve closer calibration to experiment for both parameters, despite having fewer degrees of freedom for calibration than the R-ϕ-$2L$-a-$\mathcal{C}$ model. In contrast, calibration for the R-ϕ-$2L$-a-$\mathcal{C}$ model seemingly must compromise agreement with respect to experiment in one of these two parameters. For engineering problems involving turbulent mixing, it is likely more important to capture the KH growth rate than the shear stress correlation. As a result, the nominal R-ϕ-$2L$-a-$\mathcal{C}$ model coefficients given in Table I are those matching $\frac{\delta}{\mathcal{A}} = 0.08$.
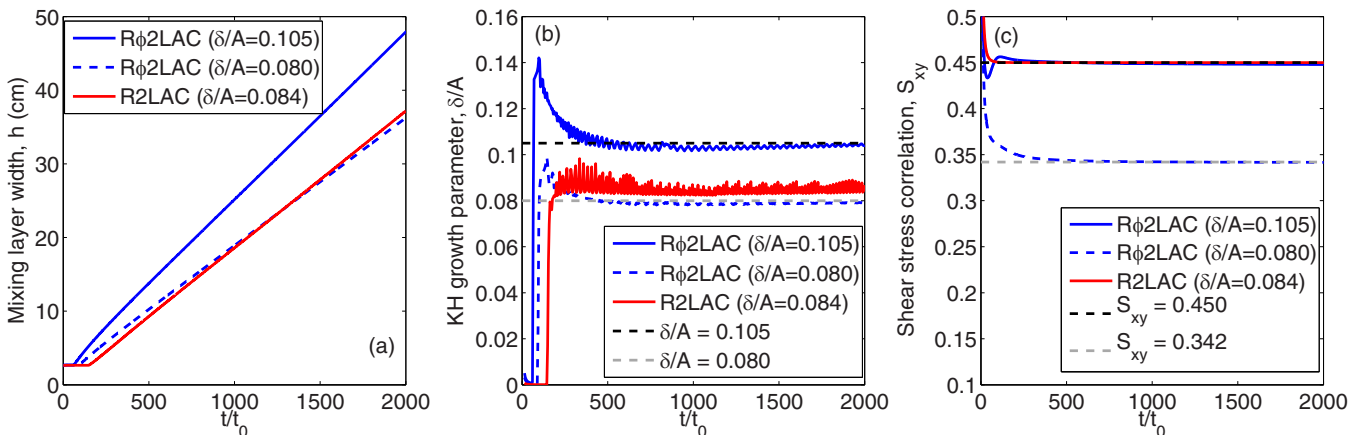
FIG. 4. Time evolution of (a) KH mixing layer width h, (b) KH growth parameter $\delta/\mathcal{A}$, and (c) shear stress correlation $\mathcal{S}_{xy}$ with both the R-$2L$-a-$\mathcal{C}$ and the R-ϕ-$2L$-a-$\mathcal{C}$ models. Two different simulations with the R-ϕ-$2L$-a-$\mathcal{C}$ models are shown, where model coefficients have been constrained for $\frac{\delta}{\mathcal{A}} = 0.080$ (solid blue) and for $\frac{\delta}{\mathcal{A}} = 0.105$ (dashed blue).
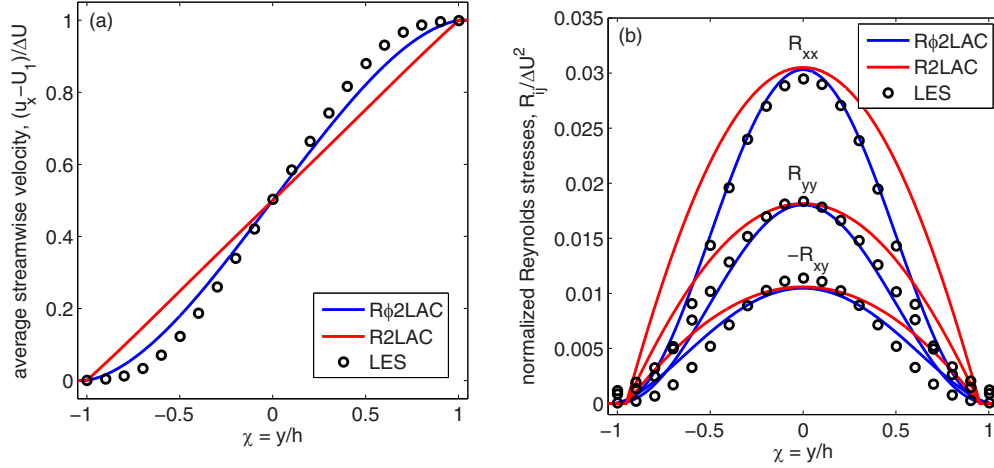
FIG. 5. Comparison of KH spatial profiles between the R-$2L$-a-$\mathcal{C}$ model, the R-ϕ-$2L$-a-$\mathcal{C}$ model, and LES by Morgan [37]: (a) average streamwise velocity $\frac{\widetilde{u}_x - U_1}{\Delta U}$ and (b) normalized Reynolds stresses $R_{ij}/\Delta U^2$ are plotted vs the spatial similarity variable $\chi = x/h$. R-ϕ-$2L$-a-$\mathcal{C}$ results shown using model coefficients constrained for $\frac{\delta}{\mathcal{A}} = 0.105$.

Spatial profiles of the streamwise velocity $\widetilde{u}_x$ and Reynolds stresses are compared among the R-$2L$-a-$\mathcal{C}$ model, the R-ϕ-$2L$-a-$\mathcal{C}$ model, and LES data by Morgan [37] in Fig. 5. As previously observed in the RT problem, the high-order spatial profiles of the R-ϕ-$2L$-a-$\mathcal{C}$ agree better with LES, particularly in the tails. Relative magnitudes of the three Reynolds stress components are matched well for both models with $B_{xx}^{KH} = 0.1233$ and $\mathcal{S}_{xy} = 0.45$. For the nominal R-ϕ-$2L$-a-$\mathcal{C}$ model coefficients with $\mathcal{S}_{xy} = 0.342$, relative magnitudes of R_{xx} and R_{yy} are unchanged, but magnitude of R_{xy} is underpredicted by around 20% with respect to LES. It is also worth noting that agreement in spatial profiles of R_{xx} and R_{yy} are somewhat better than agreement in R_{xy} with the R-ϕ-$2L$-a-$\mathcal{C}$ model, and agreement in the KH velocity profile is not quite as good as agreement in the RT mass fraction profile previously illustrated in Fig. 2. These differences indicate that choosing shape parameter $n_u = 3/2$ would probably give better agreement with LES; however, since n_u is constrained to be $n_Y/2$, and n_k is constrained to be $n_Y + 1$, choosing $n_u = 3/2$ would lead to degraded agreement in profiles of $\widetilde{Y}_H$ and the isotropic Reynolds stresses.

C. 2D tilted rocket rig

The 1D RT and KH problems are useful to assess self-similar model behavior; however, multidimensional simulation is required to assess the impact of anisotropic diffusion. The tilted rocket rig problem [44–47] is a 2D RT test problem in which the fluid interface is inclined with respect to gravity. As a result of this inclination, the interface develops in a 2D fashion with a bulk overturning motion that leads to the development of large-scale bubble and spike features in addition to fine-scale turbulent mixing.

Computational setup for this problem follows closely to LES by Ferguson *et al.* [49]. The computational domain is a rectangular box of width $L_x = 15$ cm and height $L_y = 25$ cm, with an initial interface tilt angle $\theta = 5.766°$ and gravity oriented in the positive y dimension. The heavy fluid is initially located in the lower half of the domain with heavy density

$\rho_H = 1.89$ g/cm^3 and light density $\rho_L = 0.66$ g/cm^3. Reasonable grid convergence was obtained with 528 uniformly spaced computational zones in x and 880 zones in y, leading to grid spacing of about 0.028 cm. Initial density and mass fraction profiles are taken as a step function, with initial mixing layer width assumed to be much less than the zone spacing. Turbulence variables are initialized only in zones bordering the interface and set to zero elsewhere. Following the approach of Ferguson *et al.* [49], who applied a Tukey window to interface perturbations near the right and left boundaries, an identical Tukey window of width 1.5 cm is additionally applied to initial conditions for L_t, L_d, and R_{ij} in the present RANS simulations. In order to make comparisons across several RANS models on a common footing for each RANS simulation, initial L_t is tuned to match the centerline 1%–99% average mass fraction width, h_{99}, from LES at $t/t_0 = 1.241$, where the characteristic timescale $t_0 = \sqrt{L_x/(A_T g)}$. Initial L_d is taken to match L_t, and initial Reynolds stresses are set such that initial $k = 0.01 A_T g L_t$, as suggested by Denissen *et al.* [46]. As done previously, ϕ is initialized to $\sqrt{k}$ for the R-ϕ-$2L$-a-$\mathcal{C}$ model.

Figure 6 illustrates the time evolution of mixing layer width along the centerline for the R-$2L$-a-$\mathcal{C}$ and R-ϕ-$2L$-a-$\mathcal{C}$ models. For comparison, results using the k-L-a [26] and k-$2L$-a-$\mathcal{C}$ [37,40] models are also included, along with LES results from Ferguson *et al.* [49]. As mentioned previously, the initial L_t value for each RANS model has been tuned to approximately match LES at $t/t_0 = 1.241$. Under these conditions, the k-L-a and R-$2L$-a-$\mathcal{C}$ models overpredict growth at early time to varying degrees, while the k-$2L$-a-$\mathcal{C}$ model underpredicts late-time growth. While it is not necessarily expected that the RANS results should compare well at early time when turbulence in the LES is pretransitional, it is remarkable that the R-ϕ-$2L$-a-$\mathcal{C}$ model agrees well with LES for the full time history.

Color contours of average heavy species mass fraction $\widetilde{Y}_H$ in Fig. 7 provide a qualitative overview of comparisons between several RANS model and LES. In this figure, contours are compared among the k-L-a, R-$2L$-a-$\mathcal{C}$, and R-ϕ-$2L$-a-$\mathcal{C}$
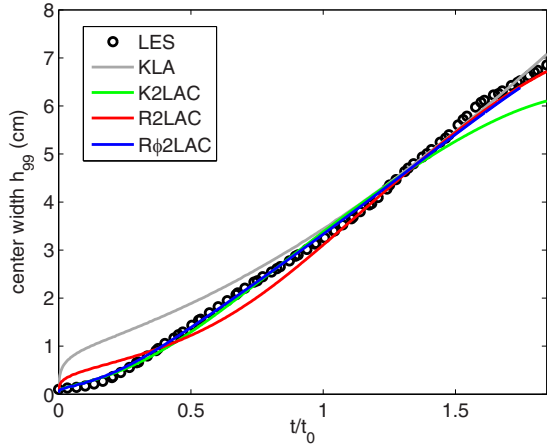
FIG. 6. Time history of centerline mixing layer width h_{99} for several RANS models in simulations of the 2D tilted rocket rig problem, compared with LES data by Ferguson *et al.* [49].

models. To assess the impact of anisotropic eddy viscosity, results using the R-$2L$-a-$\mathcal{C}$ model have been included in which an isotropic scalar eddy viscosity of the form $\mu_t = C_\mu L_t \sqrt{2k}$ has been used in Fig. 7(b), and an anisotropic tensor eddy viscosity of the form of Eq. (17) has been used in Fig. 7(c). The two RANS models with isotropic eddy viscosity in Figs. 7(a) and 7(b) do not show much qualitative difference between them, and although they match LES mixing layer width at the centerline, the large-scale spike and bubble features appear much more diffuse than in the LES data. Moving from isotropic eddy viscosity in Fig. 7(b) to anisotropic eddy viscosity in Fig. 7(c) results in subtle but noticeable differences in the formation of the large-scale features, particularly in the spike feature on the left boundary. In Fig. 7(c) the spike feature is less diffuse than in Figs. 7(a) or 7(b), and it reaches slightly higher along the y axis. The R-ϕ-$2L$-a-$\mathcal{C}$ model in Fig. 7(d) demonstrates additional improvement in the resolution of this spike feature, matching most closely with the LES in its overall width and height. Interestingly

with the R-ϕ-$2L$-a-$\mathcal{C}$ model, the bubble feature along the right boundary is less diffuse than with the other models, and it is observed to pull away from the wall more than in the LES. It is worth noting, however, that details of the spike and bubble features appear somewhat sensitive to the choice of initial perturbations in LES, and bubble behavior similar to what is seen in Fig. 7(d) has been observed in both experimental imaging and in prior simulations of the tilted rocket rig (see, for instance, Fig. 1 in Ferguson *et al.* [49] or Fig. 2 in Denissen *et al.* [46]). In RANS simulations, the formation of these spike and bubble features seems to be primarily determined by the magnitude and distribution of horizontal mass flux, which is a function of both initial conditions and model form. By calibrating initial conditions to match LES mixing layer width, however, we have attempted to focus this comparison on model form differences.

Figure 8 further explores comparisons of average mass fraction profiles by overplotting contours of $\widetilde{Y}_H$ from LES with those from the RANS simulations previously shown in Figs. 7(b) through 7(d). Considering first comparisons between LES and the RANS models away from the boundaries, Fig. 8 illustrates that all three RANS results agree with LES in the total width, as expected. Agreement appears somewhat better with the R-ϕ-$2L$-a-$\mathcal{C}$ model than with the other two RANS models in comparison of internal contours; this agreement is most noticeable at upper edge of the mixing layer with the R-ϕ-$2L$-a-$\mathcal{C}$ model. Inset images in Figs. 8(a) through 8(c) illustrate contour comparisons in the area immediately around the spike feature. From these inset images, improving agreement in the formation of the spike becomes most noticeable. Anisotropic eddy viscosity with the R-$2L$-a-$\mathcal{C}$ model results in improved agreement over isotropic eddy viscosity with the same model, and the R-ϕ-$2L$-a-$\mathcal{C}$ model then results in additional improvement over the R-$2L$-a-$\mathcal{C}$ model.

Contours of the transverse mass flux velocity a_x are compared in Fig. 9 between LES and three R-ϕ-$2L$-a-$\mathcal{C}$ simulations with varying values of the model coefficient C_{A2}. Ferguson *et al.* showed that the C_{A2} production term was the dominant contributor to the transverse mass flux budget
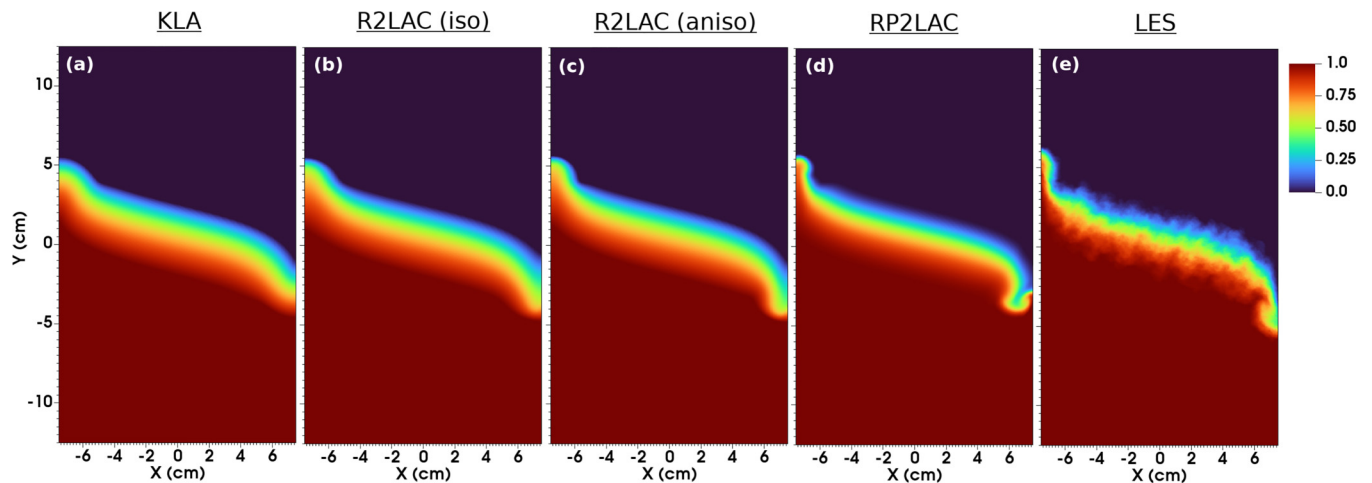
FIG. 7. Color contours of average heavy species mass fraction $\widetilde{Y}_H$ at time $t/t_0 = 1.241$ from several different simulations of the tilted rocket rig: (a) the k-L-a model, (b) the R-$2L$-a-$\mathcal{C}$ model with isotropic scalar eddy viscosity, (c) the R-$2L$-a-$\mathcal{C}$ model with anisotropic tensor eddy viscosity, (d) the R-ϕ-$2L$-a-$\mathcal{C}$ model with anisotropic tensor eddy viscosity, and (e) LES data from Ferguson *et al.* [49].
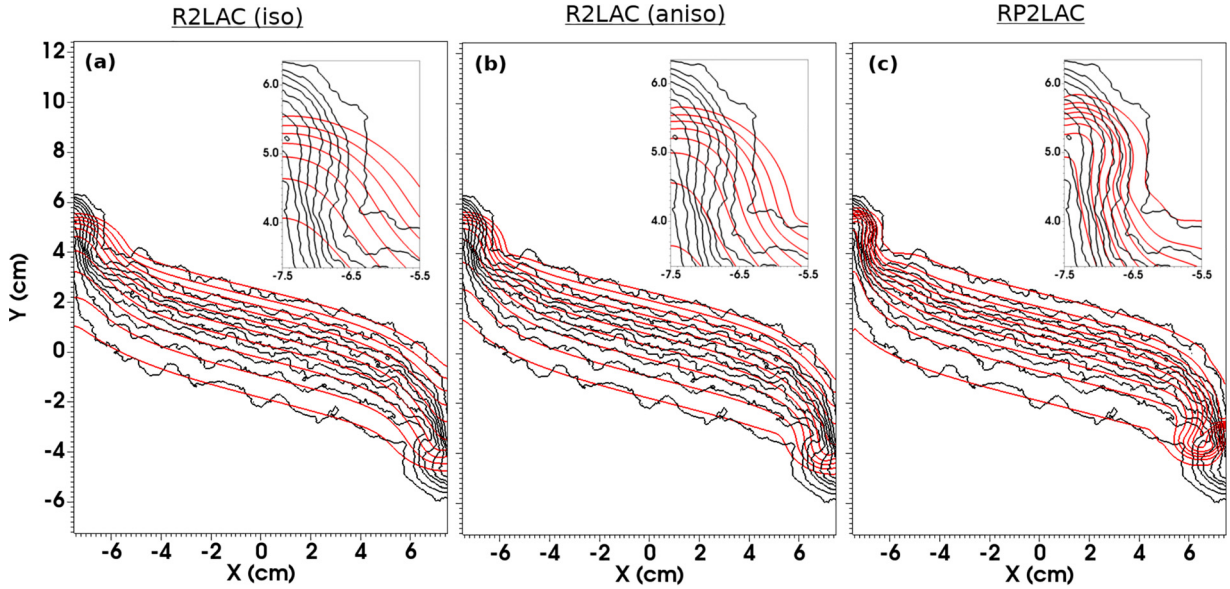
FIG. 8. First ten contours of average heavy species mass fraction $\widetilde{Y}_H$ evenly distributed between 0.01 and 0.99 at time $t/t_0 = 1.241$. Black contours from LES data by Ferguson *et al.* [49]. Red contours from RANS simulations using (a) the R-$2L$-a-$\mathcal{C}$ model with isotropic scalar eddy viscosity, (b) the R-$2L$-a-$\mathcal{C}$ model with anisotropic tensor eddy viscosity, and (c) the R-ϕ-$2L$-a-$\mathcal{C}$ model with anisotropic tensor eddy viscosity. Inset images show contours zoomed in near the spike feature on the left-hand side.

in their LES calculations, but this term disappears from the 1D similarity analysis discussed previously in Sec. III. As Figs. 9(a) through 9(c) illustrate, decreasing C_{A2} from 0.75 to 0.15 brings the magnitude of a_x into better agreement with LES. On the other hand, inset images comparing average mass fraction contours in Figs. 9(a) through 9(c) also illustrate that as C_{A2} is reduced in this way, agreement in the details of the spike feature actually degrades. Indeed, negative a_x indicates mass flux towards the left wall; so a trend of increasing a_x intuitively should correspond to a less compacted spike as more mass is moving away from the left wall. The fact that simultaneous agreement in both spike formation and a_x magnitude could not be achieved in Fig. 9 indicates that improvement

could potentially be obtained by optimizing the self-similar scaling ratio A_0^2/R_0.

D. Shock-accelerated turbulent patch

The shock-accelerated turbulent patch problem is a 2D RM test problem proposed by Olson and Williams [48] in which a fluid interface with localized surface perturbations is subjected to a planar shock wave. In contrast to the more canonical 1D RM problem in which surface perturbations are homogeneous across the fluid interface, the heterogeneity of the interface in the turbulent patch problem leads development of a highly anisotropic plume.
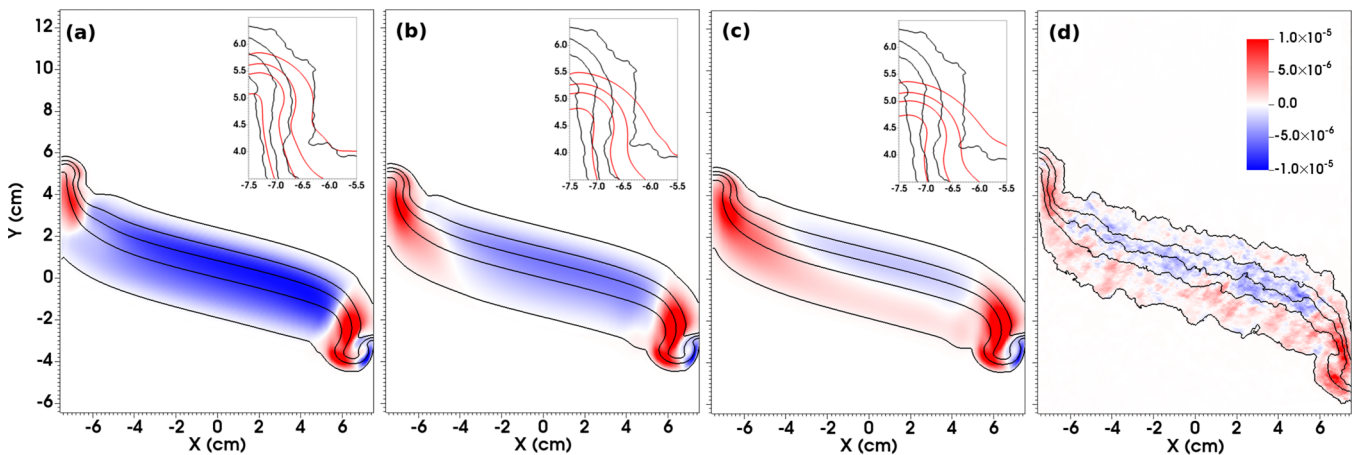
FIG. 9. Color contours of transverse mass flux velocity a_x (units of cm/μs) at time $t/t_0 = 1.241$ for several tilted rocket rig simulations using the the R-ϕ-$2L$-a-$\mathcal{C}$ model with varying C_{A2} compared with LES data from Ferguson *et al.* [49]: (a) $C_{A2} = 0.75$, (b) $C_{A2} = 0.35$, (c) $C_{A2} = 0.15$, and (d) LES contours. Overlaid black contours indicate the first five contours of heavy species mass fraction $\widetilde{Y}_H$ evenly distributed between 0.01 and 0.99. Inset images in (a)–(c) compare $\widetilde{Y}_H$ contours from R-ϕ-$2L$-a-$\mathcal{C}$ model (in red) with contours from LES (in black) near the spike feature on the left-hand side.
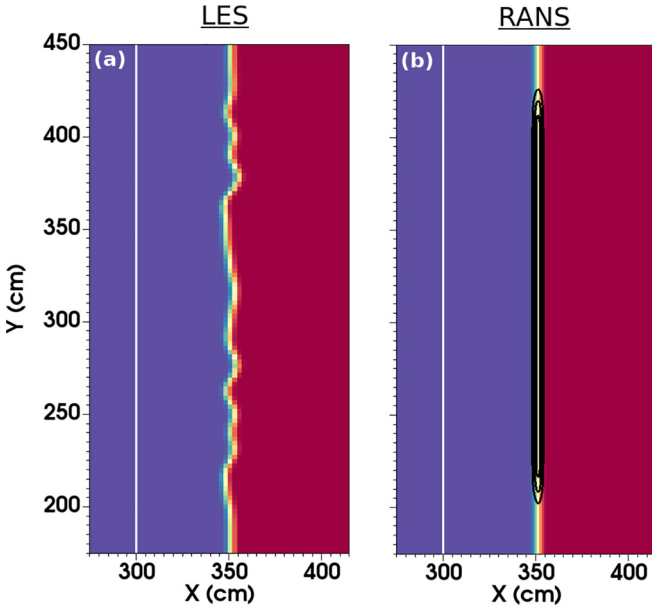
FIG. 10. Initial conditions in the shock-accelerated turbulent patch problem. (a) 2D slice through 3D instantaneous mass fraction contours Y_H from LES by Olson and Williams [48]. (b) Contours of average mass fraction $\widetilde{Y}_H$ from present RANS calculations. White contour at $x = 300$ cm indicates initial location of the shock wave, and black contours illustrate initial distribution of turbulence length scale L_t.

RANS simulations in this section are performed on a uniformly spaced mesh with 360 zones in x and 256 zones in y, on a domain of size $2.8\pi \times 2\pi$ m. A Mach 1.84 shock is driven from the heavy fluid ($\rho_H = 3$ mg/cm^3) into the light fluid ($\rho_L = 1$ mg/cm^3), with an initial interface located at $x_{\text{int}} = 3.5$ m. Both fluids are taken to be ideal gases with heat capacity ratio $\gamma = 5/3$. Following the approach of Olson and Williams [48], time-dependent sponge boundary conditions are used at the $x = 0$ and $x = 2.8\pi$ boundaries to prevent reflections, while the $y = 0$ and $y = 2\pi$ boundaries are treated

as periodic. The fluid interface is initialized with a diffuse error function profile of width $W_0 = \frac{\pi}{64}$ m,

$$\widetilde{Y}_L = \frac{1}{2}\text{erf}\left(\frac{\sqrt{\pi}(x - x_{\text{int}})}{W_0}\right). \tag{88}$$

To simulate the localized perturbations, turbulence quantities are initialized only in a patch of height $H_0 = 0.68\pi$ m such that for an arbitrary turbulence variable f, with a peak initial magnitude of f_0, an initial profile is given by

$$f = 2f_0\widetilde{Y}_H\widetilde{Y}_L\left[1 + \tanh\left(\frac{\frac{H_0}{2} - |y - \pi|}{0.05H_0}\right)\right]. \tag{89}$$

Equation (89) allows initial turbulence quantities to go smoothly to zero away from the patch in both y and x. Turbulence length scales are both initialized using Eq. (89) with peak $L_t = L_d = W_0$, and $\mathcal{C}_{HL}$ is initialized using Eq. (89) with a peak value of -0.25. Figure 10 provides a general illustration of the initial configuration for the problem. Turbulence quantities are localized within a small, smooth patch on the interface at x_{int}, which is expected to develop in a 2D way following passage of the shock wave. Comparisons in this section are taken at nondimensional time $\tau = t\dot{W}_0/\lambda_0 = 2.4$, where the characteristic length scale λ_0 and growth rate $\dot{W}_0$ are the same as those used by the so-called θ-group collaboration [59].

Figure 11 compares the plume that is obtained at $\tau = 2.4$ among several different RANS models with LES data from Olson and Williams [48] by overplotting average mass fraction contours $\widetilde{Y}_H$ from LES on top of color contours from RANS. As seen in Figs. 11(a) and 11(b) the k-L-a and k-$2L$-a-$\mathcal{C}$ models, which both utilize a Boussinesq Reynolds stress closure of the form of Eq. (1), fail to develop the plumelike structure of the LES. In contrast, the R-$2L$-a-$\mathcal{C}$ and R-ϕ-$2L$-a-$\mathcal{C}$ models, illustrated in Figs. 11(c) through 11(f), roughly capture the extent of the plume. Additionally, the two RST models are each applied to this problem with both scalar isotropic eddy viscosity of the form $\mu_t = C_\mu L_t\sqrt{2k}$ and anisotropic tensor eddy viscosity of the form of Eq. (17)
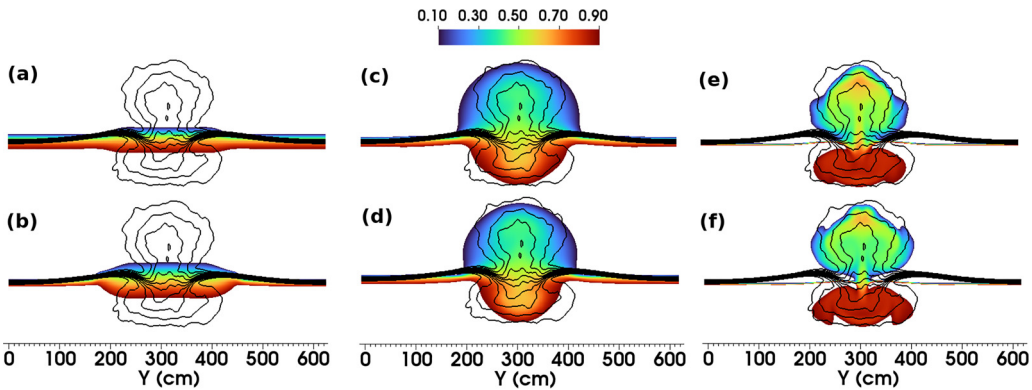
FIG. 11. Comparison of average mass fraction contours $\widetilde{Y}_H$ among several different RANS models and LES at time $\tau = 2.4$. Black contours are the first ten evenly spaced contours of $\widetilde{Y}_H$ between 0.1 and 0.9 from LES by Olson and Williams [48]. Color contours illustrate present RANS results using (a) the k-L-a model, (b) the k-$2L$-a-$\mathcal{C}$ model, (c) the R-$2L$-a-$\mathcal{C}$ model with isotropic scalar eddy viscosity, (d) the R-$2L$-a-$\mathcal{C}$ model with anisotropic tensor eddy viscosity, (e) the R-ϕ-$2L$-a-$\mathcal{C}$ model with isotropic scalar eddy viscosity, and (f) the R-ϕ-$2L$-a-$\mathcal{C}$ model with anisotropic tensor eddy viscosity.
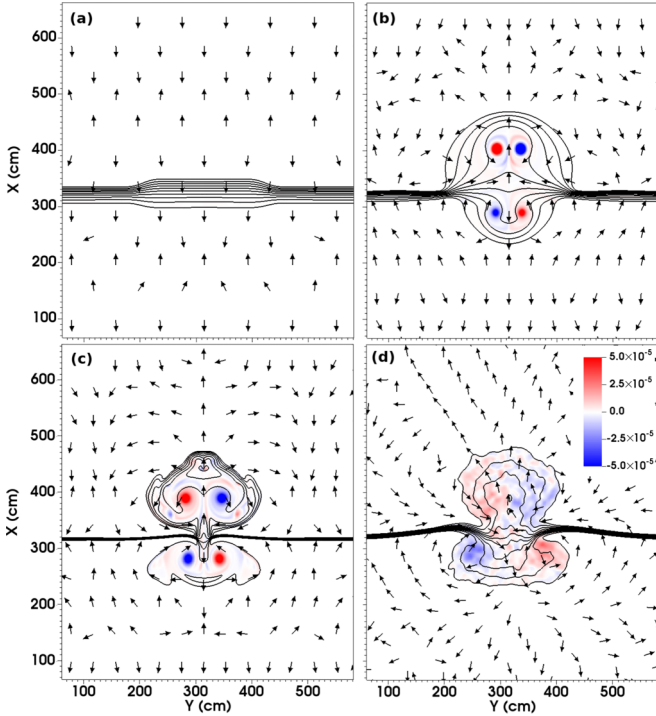
FIG. 12. Vorticity in the shock-accelerated turbulent patch problem at time $\tau = 2.4$ compared among: (a) the k-L-a model, (b) the R-$2L$-a-$\mathcal{C}$ model, (c) the R-ϕ-$2L$-a-$\mathcal{C}$ model, and (d) LES by Olson and Williams [48]. Color contours of 2D vorticity $\widetilde{\omega}_z$ (in units of $\mu\,\mathrm{s}^{-1}$) are superimposed on the first ten evenly spaced contours of $\widetilde{Y}_H$ between 0.1 and 0.9 in black. Arrows indicate direction of mean velocity vectors.

or Eq. (31). Comparing Fig. 11(c) with 11(d) and Fig. 11(e) with 11(f) reveals only minor difference in the structure of the plume as a result of the choice for eddy viscosity. It is therefore concluded that the improved agreement with the RST models over the Boussinesq models is due to the treatment of the Reynolds stress, rather than the eddy viscosity. Finally, by comparing results in Fig. 11(d) with 11(f), it seems that the R-ϕ-$2L$-a-$\mathcal{C}$ does a better job of matching the overall shape of the plume than the R-$2L$-a-$\mathcal{C}$ model, which appears to miss the pinching of contours near the base of the plume.

To better understand the nature of the average flowfield that leads to the development of the plume, Fig. 12 compares contours of 2D vorticity given by

$$\widetilde{\omega}_z = \frac{\partial \widetilde{u}_y}{\partial x} - \frac{\partial \widetilde{u}_x}{\partial y}. \tag{90}$$

Additionally in Fig. 12, arrows indicate the direction of the average velocity vector. Note that the vorticity given by Eq. (90) and plotted in Fig. 12 is the vorticity of the mean velocity, rather than the mean of the vorticity. Comparing the k-L-a model in Fig. 12(a) with the RST models in Figs. 12(b) and 12(c), it is clear that the RST models develop a pair of counter-rotating vortex cores which shape the mean velocity field and which is absent from the Boussinesq result. Although the magnitude of this vorticity is overpredicted with respect to LES, as illustrated in Fig. 12(d), the qualitative behavior of

the mean velocity field is generally well captured by the RST models.

Finally, in Fig. 13 the streamwise Reynolds stress anisotropy B_{xx} is visualized for the two RST RANS models and compared with LES. In all three cases, B_{xx} is found to reach a peak value of around $1/3$ at the farthest extents of both the spike and bubble sides of the plume. Although the RANS models both predict a slightly negative anisotropy in the core of the plume, anisotropy in the core of the LES data is more strongly negative, reaching a value of about $-1/3$. The persistence and intensity of this anisotropy even at late time reinforces the idea that Reynolds stress transport is necessary in a RANS model for the formation of the counter-rotating vortex cores observed previously in Fig. 13, and the formation of these vortex cores is ultimately the mechanism that drives development of the plume.

V. SUMMARY AND CONCLUSIONS

The present work has presented two new RST models with anisotropic eddy viscosity, referred to as the R-$2L$-a-$\mathcal{C}$ and the R-ϕ-$2L$-a-$\mathcal{C}$ models. Self-similarity analysis was performed to derive algebraic constraints on model coefficients, and a complete set of constraints was obtained for both models to reproduce expected self-similar behaviors for canonical RT, KH, and HIT problems. Self-similarity results were verified by applying the new models in simulation of 1D RT and quasi-1D KH flow. Anticipated self-similar growth parameters, anisotropies, and mixedness behavior was recovered for both problems. Although it was determined that a degeneracy of constraints exists for the KH growth parameter $\delta/\mathcal{A}$, the shear stress correlation $\mathcal{S}_{xy}$, and the anisotropy B_{xx}^{KH}, it was found that a reasonable calibration for all three parameters could still be obtained with both models. Additionally, the high-order spatial profiles of the R-ϕ-$2L$-a-$\mathcal{C}$ models were found to be in better agreement with LES data than the low-order profiles of the R-$2L$-a-$\mathcal{C}$ model. In spite of this improved agreement in the spatial profiles, given the fact that ϕ appears in a number of denominators throughout the R-ϕ-$2L$-a-$\mathcal{C}$ model equations, there exists the potential for reduced numerical stability with the R-ϕ-$2L$-a-$\mathcal{C}$ model in some problems, and in these cases the relatively simpler R-$2L$-a-$\mathcal{C}$ model might be more a more desirable option.

The new models were next assessed by applying them to the 2D inclined RT problem known as the "tilted rocket rig." In this problem, the details of the large-scale spike and bubble features were found to be sensitive to model form, and by comparing the R-$2L$-a-$\mathcal{C}$ model using with an isotropic scalar eddy viscosity to the same model with an anisotropic tensor eddy viscosity, it was found that the anisotropic tensor eddy viscosity led to improved agreement with LES in the width and height of the spike feature. Results with the R-ϕ-$2L$-a-$\mathcal{C}$ model showed further improvement in the spike feature, matching the most closely with LES. Comparisons of the transverse mass flux velocity a_x highlighted the importance of this quantity to the formation of the spike, and variation in the magnitude of the unconstrained model coefficient C_{A2} demonstrated the importance of a previously neglected production term to the evolution of the mass flux. Although a value of $C_{A2} = 0.15$ was found to
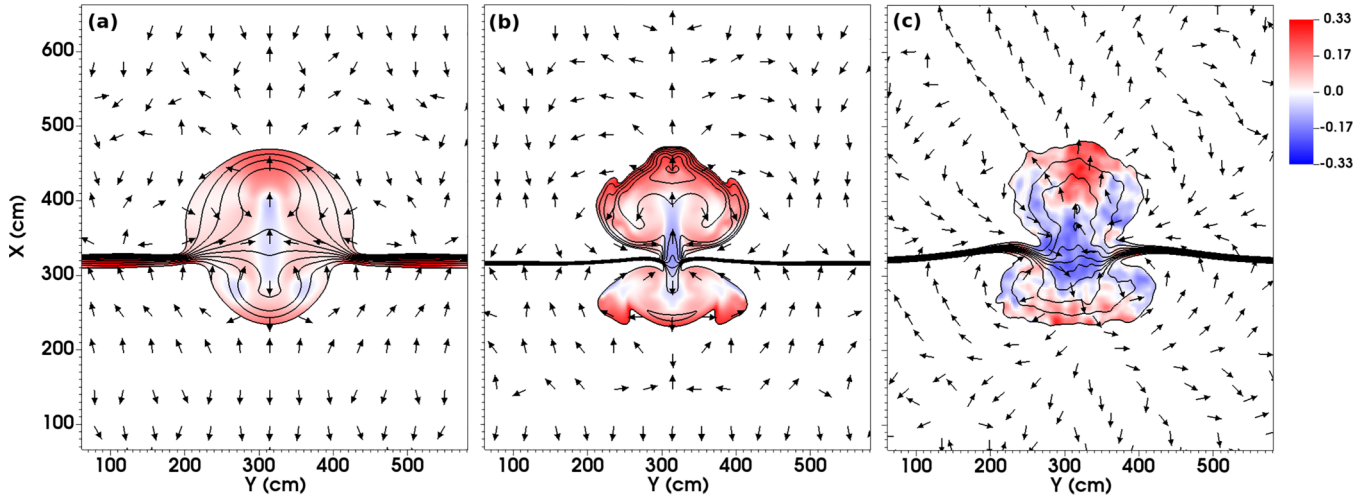
FIG. 13. Streamwise Reynolds stress anisotropy B_{xx} in the shock-accelerated turbulent patch problem at time $\tau = 2.4$ compared among (a) the R-2L-a-$\mathcal{C}$ model, (b) the R-ϕ-2L-a-$\mathcal{C}$ model, and (c) LES by Olson and Williams [48]. Color contours of B_{xx} are superimposed on the first ten evenly spaced contours of $\widetilde{Y}_H$ between 0.1 and 0.9 in black. Arrows indicate direction of mean velocity vectors.

match most closely with LES in the magnitude of a_x, a value of $C_{A2} = 0.75$ matched more closely in the shape of the spike.

Finally, the new models were applied in simulation of the shock-accelerated turbulent patch problem described previously by Olson and Williams [48]. It was found that while Boussinesq Reynolds stress models were completely unable capture the development of a turbulent plume, the RST models agreed reasonably well with LES in the shape and size of the plume. While the R-2L-a-$\mathcal{C}$ model failed to capture the pinching the base of the plume present in the LES, the R-ϕ-2L-a-$\mathcal{C}$ was able to capture this behavior. By considering spatial profiles of vorticity and streamwise Reynolds stress anisotropy, it was determined that Reynolds stress transport is necessary in a RANS model for the formation of the counter-rotating vortex cores in the shock-accelerated turbulent patch problem, and the formation of these vortex cores is ultimately the mechanism that drives development of the plume.

Models such as those presented here represent one approach for improved RANS prediction in problems of turbulent mixing involving strong anisotropies. While RANS model complications such as Reynolds stress transport and anisotropic eddy viscosity may not be necessary for good agreement in all problems of turbulent mixing, the present work suggests that they may be beneficial in ICF applications involving localized mixing around features such as fill tubes or tent perturbations. Similarly, the present work on the tilted rocket rig problem suggests potential improvement in wall-bounded turbulent mixing problems. Of course, application of the proposed models in an ICF design context remains to be shown and should be pursued in future work.

APPENDIX: SELF-SIMILARITY OF THE R-2L-a-$\mathcal{C}$ MODEL

1. Self-similarity of an RT mixing layer

At a high level, self-similarity analysis for the R-2L-a-$\mathcal{C}$ model follows a similar procedure to the analysis for the R-ϕ-2L-a-$\mathcal{C}$ model described in Sec. III. As before, a change of variable is introduced in terms of the mixing layer half-width h such that $\chi \equiv x/h$. Simpler spatial profiles are assumed such that the heavy mass fraction profile across the mixing layer is given by

$$Y_H(\chi) = \tfrac{1}{2}(1 + \chi), \tag{A1}$$

and the turbulence variables are separable according to

$$R_{xx}(\chi, t) = R_0(t)f(\chi), \tag{A2a}$$

$$L_t(\chi, t) = L_{t0}(t)f^{1/2}(\chi), \tag{A2b}$$

$$L_d(\chi, t) = L_{d0}(t)f^{1/2}(\chi), \tag{A2c}$$

$$a(\chi, t) = A_0(t)f(\chi), \tag{A2d}$$

$$\mathcal{C}_{\alpha\beta}(\chi, t) = -V_0(t)f(\chi). \tag{A2e}$$

The separability ansatz for the reduced Eqs. (8) through (11) and Eqs. (13) through (15) is satisfied with these simplified spatial profiles for

$$N_a = N_R = N_e = N_Y = N_C = 2N_{Lt}, \tag{A3a}$$

$$N_{Ld} = N_{Lt}. \tag{A3b}$$

As before, the turbulence length scale is related to the mixing layer half-width through $L_{t0} = \beta h$, and satisfaction of the separability ansatz in the reduced Eq. (12) requires

$$\beta = \sqrt{\frac{C_{L1}N_{Lt}}{2C_\mu \sqrt{\frac{1}{3} + B_{xx}^{RT}}}}. \tag{A4}$$

From the reduced L_d equation, it is found for 1D RT with the R-$2L$-a-$\mathcal{C}$ model, $L_{t0} = L_{d0}$. Simultaneous satisfaction of the reduced Eq. (11) for both R_{xx} and R_{yy} requires

$$C_{R4} = \tfrac{1}{2}C_{R3} \tag{A5}$$

and

$$B_{xx}^{RT} = \tfrac{2}{3}(1 - C_{R1}). \tag{A6}$$

Then, by imposing the constraint that $\frac{\partial}{\partial t}\left(\frac{R_0}{A_0^2}\right) = 0$, from the reduced Eq. (14), the following constraint on C_A is obtained:

$$\frac{C_A}{C_{L1}} = \frac{1}{2}\frac{C_{R3}}{C_{L1}} - \frac{1}{4} + \frac{3 - 2C_{R1}}{24\alpha_b\left(1 + \frac{C_{R3}}{C_{L1}}\right)}. \tag{A7}$$

Substituting the linear profile given by Eq. (A1) into Eq. (48) leads to the following for the R-$2L$-a-$\mathcal{C}$ model:

$$V_0 = \frac{1 - \Theta_{RT}}{4}. \tag{A8}$$

Then, utilizing the reduced Eq. (15) and recognizing $\dot{V}_0 = 0$ gives the following constraint on C_{C3}:

$$C_{C3} = \frac{1}{1 + \frac{C_{R3}}{C_{L1}}}\left(\frac{C_{C2}}{C_{L1}} + \frac{1}{2} - \frac{C_{C1}N_{Lt}}{8V_0}\right). \tag{A9}$$

Then, to obtain a constraint on N_{Lt}, the energy balance within an RT mixing layer is considered. The turbulent kinetic energy generated within an RT mixing layer is be given by

$$E_K = \int_{-h}^{h} \overline{\rho}k(x,t)\,dx = \frac{4}{1 + 3B_{xx}^{RT}}hR_0. \tag{A10}$$

As before, the gravitational potential energy within the RT mixing layer is derived by imagining a material interface at $x = 0$ and integrating over a distance $2d$. Then, evaluating Eq. (56) and considering only the difference over the mixing width $-h \leqslant x \leqslant h$ gives the change in potential energy over the mixing layer as

$$\Delta\mathrm{PE} = \frac{g}{6}(\rho_H - \rho_L)h^2. \tag{A11}$$

Thus, the fraction of potential energy converted to kinetic energy can be expressed:

$$\frac{E_K}{\Delta\mathrm{PE}} = \frac{16N_{Lt}\alpha_b}{C_\mu C_{L1}}\sqrt{\frac{1}{\frac{1}{3} + B_{xx}^{RT}}}. \tag{A12}$$

2. Self-similarity of a KH mixing layer

To obtain constraints on shear production terms, the case of a quasi-1D shear layer is again considered with a linear spatial

profile defined according to

$$\widetilde{u}_x(\chi) = \begin{cases} U_2, & \chi \geqslant 1 \\ U_1 + \frac{\Delta U}{2}(\chi + 1), & -1 < \chi < 1 \\ U_1, & \chi \leqslant -1. \end{cases} \tag{A13}$$

Following a similar approach as before, it is assumed $L_{t0} = \beta h$. Then satisfaction of the similarity ansatz in the reduced L_t equation requires

$$\beta^2 - \frac{N_{Lt}C_{L3t}\mathcal{S}_{xy}}{2C_\mu}\left(\frac{1}{3} + B_{xx}^{KH}\right)\frac{\Delta U}{\sqrt{R_0}}\beta$$
$$- \frac{C_{L1}N_{Lt}}{2C_\mu\sqrt{\frac{1}{3} - \frac{B_{xx}^{KH}}{2}}} = 0. \tag{A14}$$

As before, simultaneous satisfaction of the reduced R_{xy}, R_{xx}, and R_{yy} equations requires

$$B_{xx}^{KH} = \tfrac{2}{3}(1 - C_{R2}) \tag{A15}$$

and

$$\mathcal{S}_{xy}^2 = \frac{3B_{xx}^{KH} - \frac{9}{2}\left(B_{xx}^{KH}\right)^2}{\frac{4}{3} + 2B_{xx}^{KH} - 6\left(B_{xx}^{KH}\right)^2}. \tag{A16}$$

Notice that Eqs. (A15) and (A16) indicate that both B_{xx}^{KH} and $\mathcal{S}_{xy}$ are fully constrained by the single model coefficient C_{R2}. Comparing Eq. (A16) with Eq. (68), however, illustrates how the R-ϕ-$2L$-a-$\mathcal{C}$ model has one more degree of freedom in this regard compared to the R-$2L$-a-$\mathcal{C}$ model, due to the presence of the ratio $\frac{R_0}{P_0^2}$ in Eq. (68). Utilizing $L_{t0} = \beta h$ with the reduced L_t equation then gives the following expression for the KH growth parameter:

$$\frac{\delta}{\mathcal{A}} = 8\mathcal{S}_{xy}\frac{R_0}{\Delta U^2}\sqrt{\frac{\frac{1}{3} - \frac{B_{xx}^{KH}}{2}}{\frac{1}{3} + B_{xx}^{KH}}}, \tag{A17}$$

where the ratio $\frac{R_0}{\Delta U^2}$ is obtained by substituting into the reduced L_d equation according to

$$\frac{R_0}{\Delta U^2} = \frac{1 + C_{L3d}\frac{C_{R3}}{C_{L1}}}{8\left(\frac{C_{R3}}{C_{L1}} + \frac{1}{2}\right)}\left(\frac{1}{3} + B_{xx}^{KH}\right). \tag{A18}$$

Note that Eqs. (A17) and (A18) indicate that only a the additional model coefficient C_{L3d} is available to set both $\frac{\delta}{\mathcal{A}}$ and $\frac{R_0}{\Delta U^2}$. It is again worth noting that this coefficient degeneracy does not exist in the k-$2L$-a-$\mathcal{C}$ model. However, as illustrated in Sec. IV B, it is fortuitously possible to obtain reasonable calibration of both parameters with a single choice of C_{L3d}. Substitution into (15) then results in the reduced V_0 equation, which is rearranged to obtain

$$C_{C1} = 4V_0\left[\frac{C_{C2}}{C_\mu\beta^2}\sqrt{\frac{1}{\frac{1}{3} - \frac{B_{xx}^{KH}}{2}}}\frac{L_{t0}}{L_{d0}} + \frac{1}{N_{Lt}}\right], \tag{A19}$$

where the ratio $\frac{L_{t0}}{L_{d0}}$ is solved from the reduced L_d equation according to

$$\frac{L_{t0}}{L_{d0}} = \frac{\beta\sqrt{\frac{1}{3} - \frac{B_{xx}^{KH}}{2}}}{C_{L1d}}\left[8\mathcal{S}_{xy}\frac{\sqrt{R_0}}{\Delta U} - C_{L3d}\mathcal{S}_{xy}\left(\frac{1}{3} + B_{xx}^{KH}\right)\frac{\Delta U}{\sqrt{R_0}}\right]. \tag{A20}$$

TABLE II. Nominal R-$2L$-a-$\mathcal{C}$ model coefficients and the self-similarity parameters that constrain them.

Growth parameter	Value
B_{xx}^{RT}	0.300
α_b	0.025
Θ_{RT}	0.800
$\frac{E_K}{\Delta\text{PE}}$	0.500
B_{xx}^{KH}	0.123
Θ_{KH}	0.800
$\frac{K_0}{\Delta U^2}$	0.033
$\frac{\delta}{\mathcal{A}}$	0.084
n	1.111
m	1.333
Model coefficient	**Value**
C_μ	1.000
C_{R1}	0.550
C_{R2}	0.815
C_{R3}	1.000
C_{R4}	0.500
C_{L1}	0.400
C_{L2t}	-2.791
C_{L3t}	-4.686
C_{L2d}	0.489
C_{L3d}	0.234
C_A	0.762
C_{A2}	1.000
C_{C1}	2.184
C_{C2}	1.200
C_{C3}	0.379
N_a, N_R, N_e, N_Y, N_C	0.796
N_{Ld}, N_{Lt}	0.398

Finally, solving quadratic Eq. (A14) for β and substituting into Eq. (9) then leads to the following constraint for C_{L3t}:

$$C_{L3t}\left(\frac{1}{3} + B_{xx}^{KH}\right) = 8\frac{R_0}{\Delta U^2} - \frac{C_{L1}C_\mu}{4N_{Lt}\mathcal{S}_{xy}^2\sqrt{\frac{1}{3} - \frac{B_{xx}^{KH}}{2}}}. \quad \text{(A21)}$$

3. Decaying homogeneous isotropic turbulence

In the absence of mean velocity or pressure gradients, the model equations reduce to

$$\frac{dk}{dt} = -\frac{C_{R3}}{2}\frac{(2k)^{3/2}}{L_d}, \quad \text{(A22)}$$

$$\frac{dL_d}{dt} = C_{L1}\sqrt{2k}, \quad \text{(A23)}$$

$$\frac{dC_{\alpha\beta}}{dt} = -C_{C2}\frac{C_{\alpha\beta}\sqrt{2k}}{L_d}. \quad \text{(A24)}$$

These equations are solved in terms of a reference time, t_0, and decay exponents, n and m:

$$k = K_0\left(1 + \frac{t}{t_0}\right)^{-n}, \quad \text{(A25a)}$$

$$L_d = L_{d0}\left(1 + \frac{t}{t_0}\right)^{1-n/2}, \quad \text{(A25b)}$$

$$C_{\alpha\beta} = V_0\left(1 + \frac{t}{t_0}\right)^{-m}. \quad \text{(A25c)}$$

Substituting Eqs. (A25a) through (A25c) back into Eqs. (A22) through (A24) leads to the following constraints after some algebra:

$$\frac{C_{R3}}{C_{L1}} = \frac{2n}{2-n}, \quad \text{(A26)}$$

$$\frac{C_{C2}}{C_{L1}} = \frac{2m}{2-n}. \quad \text{(A27)}$$

4. Summary of constraints

Equations (A3), (A5), (A6), (A7), (A9), (A12), (A15), (A18), (A17), (A19), (A21), (A26), and (A27) thus represent 18 constraints on the 18 model coefficients C_{R1}, C_{R2}, C_{R4}, C_{L1}, C_{L3t}, C_{L3d}, C_A, C_{C1}, C_{C2}, C_{C3}, N_R, N_e, N_Y, N_R, N_{Lt}, N_{Ld}, N_a, and N_C in terms of the ten self-similar growth parameters B_{xx}^{RT}, α_b, Θ_{RT}, $\frac{E_K}{\Delta\text{PE}}$, B_{xx}^{KH}, Θ_{KH}, $\frac{K_0}{\Delta U^2}$, $\frac{\delta}{\mathcal{A}}$, n, and m. Coefficients C_{L2t} and C_{L2d} are again constrained according to Eqs. (87a) and (87b), and coefficient C_{A2} is not constrained through similarity analysis. As before, coefficients C_μ and one of either C_{L1} or C_{R3} end up being free parameters that do not affect the realized self-similar behavior if the constraints above are satisfied. Thus, for simplicity we take $C_\mu = C_{R3} = 1$. Table II summarizes the nominal set of model coefficients and growth parameters used for simulations in Sec. IV.

[1] J. D. Lindl, R. L. McCrory, and E. M. Campbell, Progress toward ignition and burn propagation in inertial confinement fusion, Phys. Today **45**, 32 (1992).

[2] J. Lindl, Development of the indirect-drive approach to inertial confinement fusion and the target physics basis for ignition and gain, Phys. Plasmas **2**, 3933 (1995).

[3] L. Rayleigh, Investigation of the character of the equilibrium of an incompressible heavy fluid of variable density, Proc. R. Math. Soc. **14**, 170 (1883).

[4] G. I. Taylor, The instability of liquid surfaces when accelerated in a direction perpendicular to their plane, Proc. R. Soc. London A **201**, 192 (1950).

[5] R. D. Richtmyer, Taylor instability in shock acceleration of compressible fluids, Comm. Pure Appl. Math. **13**, 297 (1960).

[6] E. E. Meshkov, Instability of the interface of two gases accelerated by a shock wave, Sov. Fluid Dyn. **4**, 101 (1969).

[7] Y. Zhou, Rayleigh–Taylor and Richtmyer–Meshkov instability induced flow, turbulence, and mixing. I, Phys. Rep. **720–722**, 1 (2017).

[8] Y. Zhou, Rayleigh–Taylor and Richtmyer–Meshkov instability induced flow, turbulence, and mixing. II, Phys. Rep. **723–725**, 1 (2017).

[9] A. Banerjee, Rayleigh-Taylor instability: A status review of experimental designs and measurement diagnostics, ASME J. Fluids Eng. **142**, 120801 (2020).

[10] O. Schilling, Progress on understanding Rayleigh-Taylor flow and mixing using synergy between simulation, modeling, and experiment, ASME J. Fluids Eng. **142**, 120802 (2020).

[11] P. A. Bradley, J. A. Cobble, I. L. Tregillis, M. J. Schmitt, K. D. Obrey, V. Glebov, S. H. Batha, G. R. Magelssen, J. R. Fincke, S. C. Hsu *et al.*, Role of shocks and mix caused by capsule defects, Phys. Plasmas **19**, 092703 (2012).

[12] C. R. Weber, D. T. Casey, D. S. Clark, B. A. Hammel, A. MacPhee, J. Milovich, D. Martinez, H. F. Robey, V. A. Smalyuk, M. Stadermann *et al.*, Improving ICF implosion performance with alternative capsule supports, Phys. Plasmas **24**, 056302 (2017).

[13] A. G. MacPhee, V. A. Smalyuk, O. L. Landen, C. R. Weber, H. F. Robey, E. L. Alfonso, K. L. Baker, L. F. Berzak Hopkins, J. Biener, T. Bunn *et al.*, Hydrodynamic instabilities seeded by the x-ray shadow of ICF capsule fill tubes, Phys. Plasmas **25**, 082702 (2018).

[14] A. G. MacPhee, V. A. Smalyuk, O. L. Landen, C. R. Weber, H. F. Robey, E. L. Alfonso, J. Biener, T. Bunn, J. W. Crippen, M. Farrell *et al.*, Mitigation of x-ray shadow seeding of hydrodynamic instabilities on inertial confinement fusion capsules using a reduced diameter fuel fill-tube, Phys. Plasmas **25**, 054505 (2018).

[15] C. R. Weber, D. S. Clark, A. Pak, N. Alfonso, B. Bachmann, L. F. Berzak Hopkins, T. Bunn, J. Crippen, L. Divol, T. Dittrich *et al.*, Mixing in ICF implosions on the national ignition facility caused by the fill-tube, Phys. Plasmas **27**, 032703 (2020).

[16] S. Gauthier and M. Bonnet, A k-ε model for turbulent mixing in shock-tube flows induced by Rayleigh-Taylor instability, Phys. Fluids A **2**, 1685 (1990).

[17] D. C. Besnard, F. H. Harlow, R. M. Rauenzahn, and C. Zemach, Turbulence transport equations for variable-density turbulence and their relationship to two-field models, Technical Report LAUR-12303 (Los Alamos National Laboratory, 1992).

[18] A. Llor and P. Bailly, A new turbulent two-field concept for modeling Rayleigh-Taylor, Richtmyer-Meshkov, and Kelvin-Helmholtz mixing layers, Laser Part. Beams **21**, 311 (2003).

[19] O. Grégoire, D. Souffland, and S. Gauthier, A second-order turbulence model for gaseous mixtures induced by Richtmyer-Meshkov instability, J. Turbul. **6**, N29 (2005).

[20] G. Dimonte and R. Tipton, K-L turublence model for the self-similar growth of the Rayleigh-Taylor and Richtmyer-Meshkov instabilities, Phys. Fluids **18**, 085101 (2006).

[21] A. Banerjee, R. A. Gore, and M. J. Andrews, Development and validation of a turbulent-mix model for variable-density and compressible flows, Phys. Rev. E **82**, 046309 (2010).

[22] J. Griffond, O. Soulard, and D. Souffland, A turbulent mixing Reynolds stress model fitted to match linear interaction analysis predictions, Phys. Scr. **2010**, 014059 (2010).

[23] J. D. Schwarzkopf, D. Livescu, R. A. Gore, R. M. Rauenzahn, and J. R. Ristorcelli, Application of a second-moment closure model to mixing processes involving multicomponent miscible fluids, J. Turbul. **12**, N49 (2011).

[24] J. Griffond and O. Soulard, Evaluation of augmented RSM for interaction of homogeneous turbulent mixture with shock and rarefaction waves, J. Turbul. **15**, 569 (2014).

[25] I. W. Kokkinakis, D. Drikakis, D. L. Youngs, and R. J. R. Williams, Two-equation and multi-fluid turbulence models for Rayleigh-Taylor mixing, Int. J. Heat Fluid Flow **56**, 233 (2015).

[26] B. E. Morgan and M. E. Wickett, Three-equation model for the self-similar growth of Rayleigh-Taylor and Richtmyer-Meshkov instabilities, Phys. Rev. E **91**, 043002 (2015).

[27] J. D. Schwarzkopf, D. Livescu, J. R. Baltzer, R. A. Gore, and J. R. Ristorcelli, A two-length scale turbulence model for single-phase multi-fluid mixing, Flow, Turbul. Combust. **96**, 1 (2016).

[28] B. E. Morgan and J. A. Greenough, Large-eddy and unsteady RANS simulations of a shock-accelerated heavy gas cylinder, Shock Waves **26**, 355 (2016).

[29] B. E. Morgan, O. Schilling, and T. A. Hartland, Two-length-scale turbulence model for self-similar buoyancy-, shock-, and shear-driven mixing, Phys. Rev. E **97**, 013104 (2018).

[30] B. E. Morgan, B. J. Olson, W. J. Black, and J. A. McFarland, Large-eddy simulation and Reynolds-averaged Navier-Stokes modeling of a reacting Rayleigh-Taylor mixing layer in a spherical geometry, Phys. Rev. E **98**, 033111 (2018).

[31] A. Campos and B. E. Morgan, Direct numerical simulation and Reynolds-averaged Navier-Stokes modeling of the sudden viscous dissipation for multicomponent turbulence, Phys. Rev. E **99**, 063103 (2019).

[32] I. W. Kokkinakis, D. Drikakis, and D. L. Youngs, Modeling of Rayleigh-Taylor mixing using single-fluid models, Phys. Rev. E **99**, 013104 (2019).

[33] I. W. Kokkinakis, D. Drikakis, and D. L. Youngs, Two-equation and multi-fluid turbulence models for Richtmyer-Meshkov mixing, Phys. Fluids **32**, 074102 (2020).

[34] M. Xiao, Y. Zhang, and B. Tian, Unified prediction of reshocked Richtmyer-Meshkov mixing with K-L model, Phys. Fluids **32**, 032107 (2020).

[35] M. Xiao, Y. Zhang, and B. Tian, Modeling of turbulent mixing with an improved K-L model, Phys. Fluids **32**, 092104 (2020).

[36] Y. Zhang, Z. He, H. Xie, M.-J. Xiao, and B. Tian, Methodology for determining coefficients of turbulent mixing model, J. Fluid Mech. **905**, A26 (2020).

[37] B. E. Morgan, Scalar mixing in a Kelvin-Helmholtz shear layer and implications for Reynolds-averaged Navier-Stokes modeling of mixing layers, Phys. Rev. E **103**, 053108 (2021).

[38] B. E. Morgan, Self-consistent, high-order spatial profiles in a model for two-fluid turbulent mixing, Phys. Rev. E **104**, 015107 (2021).

[39] N. O. Braun and R. A. Gore, A multispecies turbulence model for the mixing and de-mixing of miscible fluids, J. Turbul. **22**, 784 (2021).

[40] B. E. Morgan, Simulation and Reynolds-averaged Navier-Stokes modeling of a three-component Rayleigh-Taylor mixing problem with thermonuclear burn, Phys. Rev. E **105**, 045104 (2022).

[41] B. E. Morgan, Large-eddy simulation and Reynolds-averaged Navier-Stokes modeling of three Rayleigh-Taylor mixing configurations with gravity reversal, Phys. Rev. E **106**, 025101 (2022).

[42] H. Xie, M. Xiao, and Y. Zhang, Predicting different turbulent mixing problems with the same k-ε model and model coefficients, AIP Adv. **11**, 075213 (2021).

[43] H. Xie, M. Xiao, and Y. Zhang, Unified prediction of turbulent mixing induced by interfacial instabilities via Besnard-Harlow-Rauenzahn-2 model, Phys. Fluids **33**, 105123 (2021).

[44] V. S. Smeeton and D. L. Youngs, Experimental investigation of turbulent mixing by Rayleigh-Taylor instability III, Technical Report O 35/87 (Atomic Weapons Establishment, 1987).

[45] M. J. Andrews and D. B. Spalding, A simple experiment to investigate two-dimensional mixing by Rayleigh-Taylor instability, Phys. Fluids **2**, 922 (1990).

[46] N. A. Denissen, B. Rollin, J. M. Reisner, and M. J. Andrews, The tilted rocket rig: A Rayleigh-Taylor test case for RANS models, ASME J. Fluids Eng. **136**, 091301 (2014).

[47] M. J. Andrews, D. L. Youngs, D. Livescu, and T. Wei, Computational studies of two-dimensional Rayleigh-Taylor driven mixing for a tilted-rig, ASME J. Fluids Eng. **136**, 091212 (2014).

[48] B. J. Olson and R. Williams, Richtmyer-Meshkov mixing layer growth from localized perturbations, in *Proceedings of the 16th International Workshop on the Physics of Compressible Turbulent Mixing* (Marseille, France, 2018), pp. 29–34.

[49] K. Ferguson, K. M. Wang, and B. E. Morgan, Mass and momentum transport in the tilted rocket rig experiment, Phys. Rev. Fluids **8**, 094502 (2023).

[50] J. R. Ristorcelli and T. T. Clark, Rayleigh-Taylor turbulence: Self-similar analysis and direct numerical simulation, J. Fluid Mech. **507**, 213 (2004).

[51] A. Banerjee, W. N. Kraft, and M. J. Andrews, Detailed measurements of a statistically steady Rayleigh-Taylor mixing layer from small to high Atwood numbers, J. Fluid Mech. **659**, 127 (2010).

[52] W. H. Cabot and A. W. Cook, Reynolds number effects on Rayleigh-Taylor instability with possible implications for type Ia supernovae, Nat. Phys. **2**, 562 (2006).

[53] B. E. Morgan, B. J. Olson, J. E. White, and J. A. McFarland, Self-similarity of a Rayleigh-Taylor mixing layer at low Atwood number with a multimode initial perturbation, J. Turbul. **18**, 973 (2017).

[54] J. H. Bell and R. D. Mehta, Development of a two-stream mixing layer from tripped and untripped boundary layers, AIAA J. **28**, 2034 (1990).

[55] G. K. Batchelor and A. A. Townsend, Decay of vorticity in isotropic turbulence, Proc. R. Soc. London A **190**, 534 (1947).

[56] G. Dimonte and M. Schneider, Density ratio dependence of Rayleigh-Taylor mixing for sustained and impulsive acceleration histories, Phys. Fluids **12**, 304 (2000).

[57] G. W. Sutton, Decay of passive scalar fluctuations in isotropic homogeneous turbulence, Phys. Fluids **11**, 671 (1968).

[58] B. E. Morgan, M. Osawe, M. Marinak, and B. J. Olson, RANSBox: A zero-dimensional modular software package for Reynolds-averaged Navier-Stokes modeling (unpublished).

[59] B. Thornber, J. Griffond, O. Poujade, N. Attal, H. Varshochi, P. Bigdelou, P. Ramaprabhu, B. Olson, J. Greenough, Y. Zhou *et al.*, Late-time growth rate, mixing, and anisotropy in the multimode narrowband Richtmyer-Meshkov instability: The θ-group collaboration, Phys. Fluids **29**, 105107 (2017).